

---

# BAYESIAN HIERARCHICAL MODELING AND ANALYSIS FOR PHYSICAL ACTIVITY TRAJECTORIES USING ACTIGRAPH DATA

---

**Pierfrancesco Alaimo Di Loro**

Dpt. of Statistical Sciences  
 University of Rome "La Sapienza"  
 pierfrancesco.alaimodiloro@uniroma1.it

**Marco Mingione**

Dpt. of Statistical Sciences  
 University of Rome "La Sapienza"  
 marco.mingione@uniroma1.it

**Jonah Lipsitt**

Fielding School of Public Health  
 University of California, Los Angeles  
 jonahlipsitt@gmail.com

**Christina M. Batteate**

Center of Occupational and Environmental Health  
 University of California, Los Angeles  
 cbatteate@ucla.edu

**Michael Jerrett**

Fielding School of Public Health  
 University of California, Los Angeles  
 mjerrett@ucla.edu

**Sudipto Banerjee**

Fielding School of Public Health  
 University of California, Los Angeles  
 sudipto@ucla.edu

December 23, 2024

## ABSTRACT

Rapid technological developments in accelerometers have generated substantial interest in monitoring human activity. Wearable devices, such as wrist-worn sensors that monitor gross motor activity (actigraph units) continuously record the activity levels of a subject, producing massive amounts of high-resolution measurements. Analyzing actigraph data needs to account for spatial and temporal information on trajectories or paths traversed by subjects wearing such devices. Inferential objectives include estimating a subject's physical activity levels along a given trajectory; identifying trajectories that are more likely to produce higher levels of physical activity for a given subject; and predicting expected levels of physical activity in any proposed new trajectory for a given set of health attributes. We devise a Bayesian hierarchical modeling framework for spatial-temporal actigraphy data to deliver fully model-based inference on trajectories while accounting for subject-level health attributes and spatial-temporal dependencies. We undertake a comprehensive analysis of an original dataset from the Physical Activity through Sustainable Transport Approaches in Los Angeles (PASTA-LA) study to formally ascertain spatial zones and trajectories exhibiting significantly higher levels of physical activity.

*Keywords:* Bayesian hierarchical models; Directed acyclic graphs; Gaussian processes; Physical activity; Sparsity; Spatial-temporal statistics.

## 1 Introduction

Promoting a healthy lifestyle continues to stoke substantial research activities in public health. The "Physical Activity Guidelines for Americans" (2nd edition) suggests that most individuals, depending on age and body composition, receive 150-300 minutes of moderate to vigorous physical activity (MVPA) weekly [Piercy et al., 2018]. In general, the scientific community agrees that regular physical activity (PA) can have immediate and long-term health benefits [Reiner et al., 2013, Bull et al., 2020]. Despite these well-known benefits, most Americans fail to meet recommended requirements [Piercy et al., 2018]. Specifically, only 1 in 5 high-school adolescents and 1 in 4 adults meet recommended levels of physical activity (PA). Given the well-established relationships between lack of PA and several obesity-related chronic conditions such as heart disease, type 2 diabetes, and cancer, as well as many physical and mental health benefits, an urgent need exists to improve monitoring of PA and to establish public health programs that promote more PA<sup>1</sup>.

---

<sup>1</sup>More details at <https://www.cdc.gov/chronicdisease/resources/publications/factsheets/physical-activity.htm>

Technologies for monitoring spatial energetics [James et al., 2016, Drewnowski et al., 2020] and promoting physical activity continue to emerge. *Actigraphy* broadly refers to the monitoring of human rest and activity cycles using wearable devices. Actigraphy data are gathered directly from wearable sensors or indirectly through smart-phone mobile applications and record repeated measurements at very high resolution. Accelerometers, in particular, are motion sensors that measure acceleration along different axes and are able to collect large amounts of data [Plasqui and Westerterp, 2007, Sikka et al., 2019]. They are increasingly conspicuous because of their affordability, accuracy, and availability in smart-phones, smart-watches and other wearable devices. Many devices include Global Positioning System (GPS) sensors that reference measurements with location tracking along trajectories, or paths, traversed by the subject. Collected data can be quickly downloaded and promptly analyzed to obtain insights into their pattern and structure.

We pursue a comprehensive analysis of an original actigraphy data set from the Physical Activity through Sustainable Transport Approaches in Los Angeles (PASTA-LA) study. Analyzing such data is sought for several reasons: (i) estimating a subject's physical activity levels along a given trajectory; (ii) identifying trajectories that are more likely to produce higher levels of physical activity for a given subject; and (iii) predicting expected levels of physical activity in any proposed new trajectory for a given set of health attributes. Researchers find actigraphy tracking especially attractive as it allows for a better understanding of what behavioral and environmental factors influence population and individual health and, hence, aid in public health recommendation and policy.

Given that actigraphs generate large amounts of spatial-temporal data, it is natural choose from the rich classes of such models [Cressie and Wikle, 2011, Gelfand et al., 2010]. However, actigraph data present some notable challenges [Kestens et al., 2017]: they exhibit dependence along trajectories and must be accounted while predicting PA along arbitrary (unobserved) trajectories. We argue against a customary spatiotemporal process over  $\mathbb{R}^2$  and disentangle spatial effects from dependence along trajectories. The balance of the paper is organized as follows. Section 2 introduces the PASTA-LA data set with insights into accelerometry data. The model for the temporal correlation is introduced in Section 3, while spatial effects are discussed in Section 3.4. An extensive simulation study validating our model is proposed in Section 3.5. Data analysis, including model assessment and comparisons, are presented in Section 4. Finally, we conclude with a discussion in Section 5.

## 2 Data

### 2.1 Data collection

Our dataset is compiled from the original **Physical Activity through Sustainable Transport Approaches in Los Angeles** (PASTA-LA) study conducted on a cohort of 460 individuals monitored between May 2017 and June 2018. Data were collected through different sources: online questionnaires, a smartphone app named *MOVES*, a GPS device (GlobalSat DG-500), and a wearable Actigraph unit (Actigraph GT3X+). We focus on the values recorded by Actigraph and GPS devices worn by 134 subjects for two one-week periods (one in 2017 and one in 2018). Study protocol for safeguarding participant information received necessary institutional review board (IRB) approval. The data were stored on a secure computer and a redacted version was created for purposes of data sharing.

**Questionnaires** The online questionnaires included two baseline and four follow-up surveys: one baseline and two follow-ups for each collection period of the actigraph and GPS data. Each survey consisted of responses pertaining to the participant's demographics and transportation habits. This survey is the *first baseline questionnaire* and contains personal information such as sex, age, BMI, ethnicity and other socioeconomic factors. A user ID was assigned to each survey response data and a redacted master key was generated using all ID types for joining with other study data.

**Actigraph** The Actigraph unit is an accelerometer roughly the same size and weight of the average wrist-watch that can be worn on the wrist, hip, and thigh and measure the directional acceleration at a pre-specified time frequency (generally 10 Hz to 30 Hz). The Actigraph GT3X+ model used for the PASTA-LA study can detect movement in up to three orthogonal planes (anteroposterior, mediolateral, and vertical). Data are stored in an internal memory and can be downloaded to other hardware for analysis through a proprietary software. During download, the software converts the raw acceleration information to activity counts, step counts, caloric expenditure, and activity levels, aggregated at the level of sample epochs that can be specified by the user. The proprietary software precludes recovering the raw data once they have been processed in the download phase.

Our study asked the 134 participants to keep the Actigraph unit on them (wrist) at all times other than during bathing and sleeping (awake time was assumed approximately from 7am to 11pm). Observations recorded outside this daily time-window were excluded. When participants arrived at the research offices to drop off devices, some described issues of efficacy in the ability to keep the device on or charged. Indeed, while the actigraphs were supposed to hold a

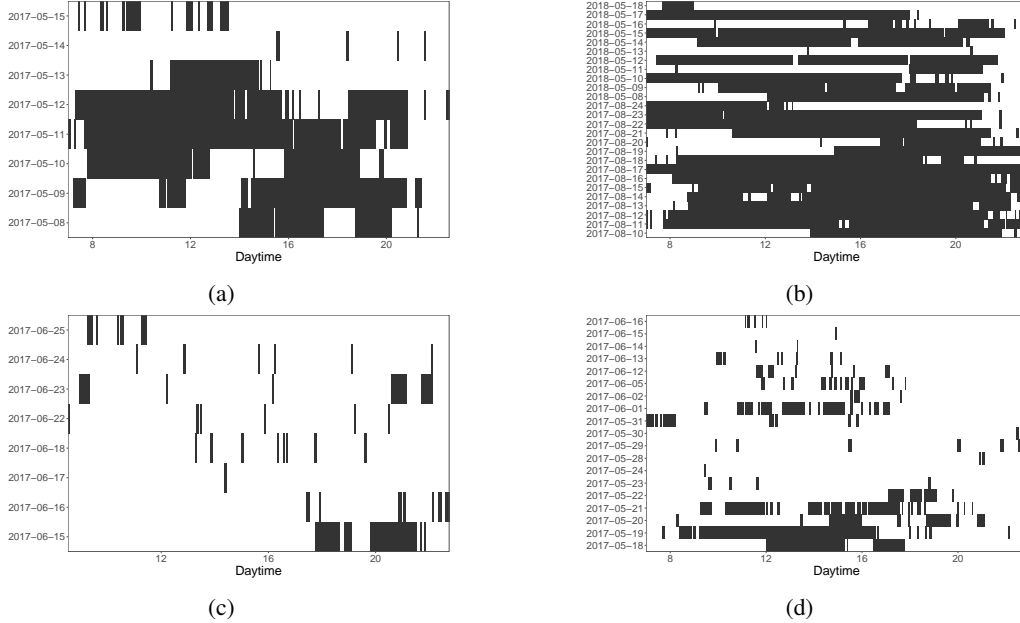


Figure 1: Derived missing data patterns for actigraph data during the daytime for 4 individuals arising from querying the inclinometer and eliminating low values: blank spots are missing data, black spots are observed values.

charge long enough to last the whole week, this was not always the case (possibly due to external conditions affecting the battery life or variations in manufacturing). This resulted in a large amount of missing data. During download the data were aggregated in sample epochs spanning 10 seconds. Measurements included the activity counts for the three axles and step counts. Time-stamps for final measurements (hour, minute, and second) were referenced by the mid-point between the beginning and the end of the epoch.

The Actigraph GT3X+ automatically records a measure of inclinometer values on how many of the 10-second epochs have been spent by the individual lying down (*inclinometer:lying*), sitting (*inclinometer:sitting*), standing (*inclinometer:standing*) or without wearing the accelerometer (*inclinometer:off*). These variables were not of primary interest to the PASTA-LA study and were not directly addressed in their data collection protocol for quality assurance. Inclinometers<sup>2</sup>, have reported sizable error rates up to 30% depending upon where they are worn and are likely less accurate when worn on the wrist [Peterson et al., 2015]. We sought to exploit convergence of accelerometry and inclinometer data to derive periods of inactivity. We checked that large values of *inclinometer:off* corresponded to low ( $\sim 0$ ) values of activity in all the possible endpoints. Then, we dropped observations with *inclinometer:off* larger than 5s (i.e., the accelerometer was inactive for more than half of the epoch). This yields “missing data” from querying the inclinometer and eliminating low values. These resulted in  $\approx 6.4 \times 10^6$  scattered observations exhibiting missingness patterns as in Figure 1.

**GPS** The *GlobalSat DG-500* was provided to the 134 subjects, which recorded the subject’s location (latitude and longitude) every 15 seconds and comprised date and time of localization and speed in kilometers per hour (computed as distance over time through linear interpolation). In order to avoid a geographical imbalance that could bias and invalidate the model estimates, for the current analysis we restricted attention to subjects living and working in the Westwood neighborhood of Los Angeles.

**Joining** GPS and accelerometer data were all assigned a participant ID aligned with the questionnaires’ master-key to facilitate joining across all ID types (including email) while redacting and encrypting user data. The first baseline questionnaire, Actigraph and GPS were available for our group of 134 individuals. Henceforth, we refer to this specific group of units. We then build two different data sets:

- The first dataset,  $D_1$ , comprising  $N \simeq 5 \times 10^6$  measurements is obtained by joining the first baseline questionnaire with Actigraph data and includes the MAG (Section 2.2) at the different timestamps and all the individual predictors, but no spatial information.

<sup>2</sup>see <https://actigraphcorp.com> for details

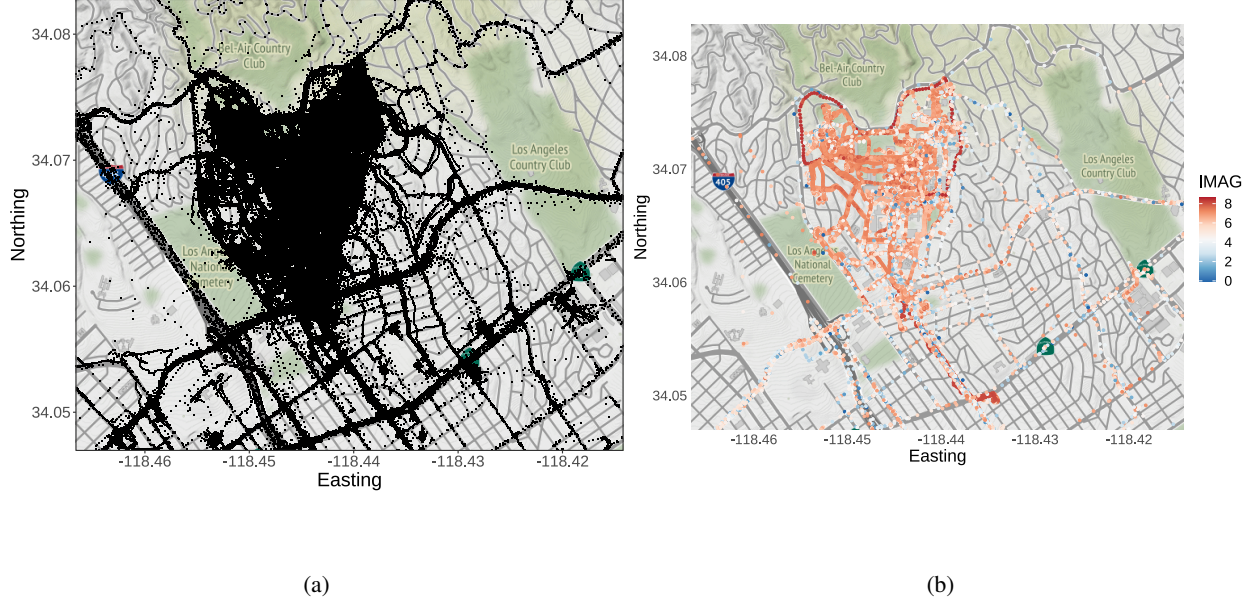


Figure 2: (a): Observed locations over the Westwood area. (b): Observed physical activity level over the Westwood area on a subset of 10 individuals

- The second dataset,  $D_2$ , consists of  $N \simeq 5 \times 10^5$  measurements (Figure 2) and is obtained by joining  $D_1$  with GPS data. Actigraph and GPS data are temporally misaligned so we joined them by linearly interpolating the GPS locations on the temporal grid from the actigraph, keeping only those interpolated values with subsequent GPS measurements less than 30 seconds apart. This is a reasonable assumption, given that the individual's trajectory is well-approximated by a piece-wise linear GPS trajectory.

## 2.2 Measure of physical activity

Our primary endpoint of analysis is the MAG (Magnitude of Acceleration) defined as:

$$MAG_{kt} = \sqrt{x_{kt}^2 + y_{kt}^2 + z_{kt}^2}, \quad k = 1, \dots, K, \quad t = t_{k1}, \dots, t_{kT}, \quad (1)$$

where  $t_{kj}$  is the  $j$ -th time point for the  $k$ -th individual; and  $x$ ,  $y$  and  $z$  are the activity counts of the three axes [Ott et al., 2000]. There are substantial investigations into the statistical relationships between accelerometer measurements and *energy expenditure* measures (EE) [Freedson et al., 2012, Taraldsen et al., 2012] and, in particular, the *Metabolic Equivalent of Task* (METs) which is currently the standard measure of *rate of activity intensity* [Crouter et al., 2006, Hall et al., 2013, Lyden et al., 2014]. *mig* [2017] offers an extensive review of proposed accelerometer measurement cut-points and transformation into physical activity metrics. More specifically, Sasaki et al. [2011], Santos-Lozano et al. [2013] and Kamada et al. [2016] investigated axis counts and vector magnitude resulting from the GT3X+ accelerometer in both controlled and free-living environments, while Aguilar-Farias et al. [2019] investigated the accuracy of relationships between MAGs and METs in comparison to those based on the vertical axis counts only and validated the results with the EE and METs as quantified by a portable calorimeter.

The MAG-to-MET relationship expounded in Sasaki et al. [2011] is expressed as a function of the MAG per minute, which we rescale to our 10 seconds aggregated counts as:

$$MET_{kt} = (0.000863 \times 6) \cdot MAG_{kt} + 0.668876, \quad (2)$$

and perform the same to the corresponding cut points for different PA intensity level (Table 1). Based upon the aforementioned literature, inference for the MAG is transformed into METs through (2) to interpret results from a physical activity perspective. Nevertheless, equations directly relating accelerometer measurements with physical activity metrics in free-living studies must be interpreted with caution. Relationships between MAG and MET have been posited in controlled studies and validated while patients are performing specific tasks (i.e. walking on a

Activity intensity	MET range	MAG
Sedentary or light	$[0, 3)$	$[0, 493)$
Moderate	$[3, 6)$	$[493, 1029)$
Hard	$[6, 9)$	$[1029, 1608)$
Very hard	$[9, \infty)$	$[1608, \infty)$

Table 1: MAG activity count cut-points for different PA intensity levels

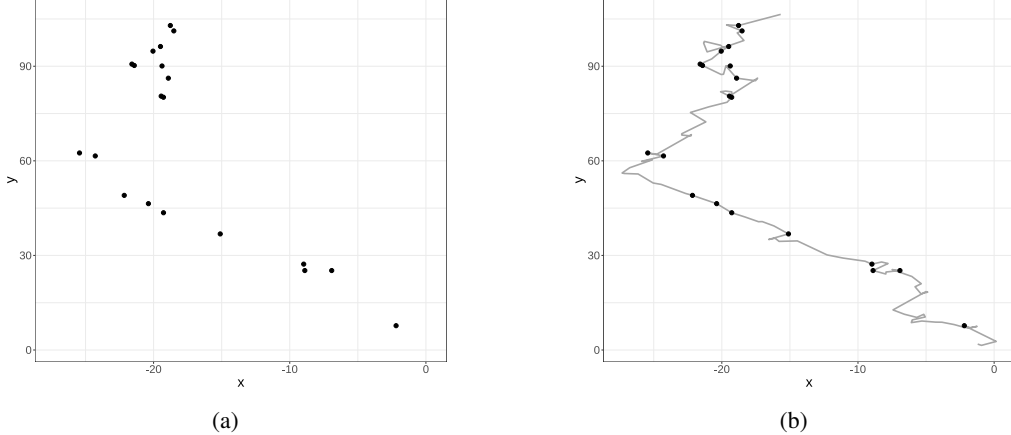


Figure 3: Example of observed points (a) and trajectory (b): black dots are realizations, grey line is domain of the process

treadmill, gardening etc.). The relationship between the recorded movement (acceleration) and the corresponding energy expenditure, can vary significantly across different tasks affecting the reliability of acceleration-based energy expenditure metrics [Lyden et al., 2011, Freedson et al., 2012, Montoye et al., 2018].

### 3 The model

The outcomes corresponding to the  $K$  subjects are referenced with respect to the time at which they are recorded and the position in the trajectory. While it is tempting to work with a spatiotemporal process, dependence introduced by such processes may not be appropriate. An individual can visit the same location numerous times in his/her trajectory. These revisits need not occur at regular intervals and can be at distant time points. This suggests that proximity of two spatial locations in a trajectory need not result in strongly dependent MAGs recorded there. It appears more reasonable to model dependence among MAG measurements through a temporal process. In fact, such temporal processes can be motivated by the position vectors defining the trajectories as we describe below.

Let  $Z_k(\cdot) : \mathbb{R}^2 \rightarrow \mathbb{R}$  be a spatial process corresponding to individual  $k$ . The domain of  $Z_k(\cdot)$  is restricted to the trajectories  $\gamma_k(t) = (\gamma_k^x(t), \gamma_k^y(t))$ , where  $k = 1, \dots, K$  and  $t \in \mathbb{R}^+$ , which defines the movements of the  $k$ -th individual along time. As shown in Figure 3, the process actually belongs to a one-dimensional space, for which we define a proper distance measure  $d(t_{ki}, t_{kj}) = \|\gamma_k(t_{kj}) - \gamma_k(t_{ki})\|$ , where  $t_{ki}$  is the  $i$ -th recorded time point from individual  $k$ . We approximate such distances as the elapsed time between the two points  $d(t_{ki}, t_{kj}) = |t_{kj} - t_{ki}|$ , which would result in a good approximation of the spatial distance (especially if the subject is moving at constant speed). More generally, the elapsed separation across time will reflect dependence better than the spatial distance. The faster an individual is moving from one point to the other, the shorter the time elapsed, and higher the correlation between the two measurements. Hence, we model our measurements as  $Y_k(\cdot) \equiv Z_k \circ \gamma_k(\cdot) : \mathbb{R}^+ \rightarrow \mathbb{R}$ , which, by construction, is a valid stochastic process.

This will form the edifice of the model in Section 3.1, where we are modeling the dependence by solely considering stochastic evolution through time. How should spatial information be introduced in the model? Two individuals at the same spatial coordinate experience the same spatial effect but different temporal effects because their physical activities are a function of their trajectory's temporal evolution. An added complication is that trajectories intersect and overlap and, in practice, can have multiple observations at the same location. Even more flexible spatiotemporal covariance kernels (e.g., nonseparable or nonstationarity) will struggle to recognize the above features. Hence, we introduce the spatial effect in the mean using *spline regression* (see Section 3.4).

### 3.1 Temporal model

Let  $\mathcal{T} = \bigcup_{k=1}^K \mathcal{T}_k$  where  $\mathcal{T}_k = \{t_{ki}\}_{i=1}^{T_k}$  and  $t_{ki} \in \mathbb{R}^+$  be the set of the  $n = \sum_{k=1}^K T_k$  observed time points. We model  $\mathbf{Y}(\mathcal{T})$  as the finite realization of a  $K$ -variate process  $\mathbf{Y}(\cdot)$  over  $\mathbb{R}^+$ :

$$\mathbf{Y}(t) = \mathbf{X}(t, \gamma(t))^\top \boldsymbol{\beta} + \mathbf{w}(t) + \boldsymbol{\varepsilon}(t), \quad t \in \mathbb{R}^+, \quad (3)$$

where  $\mathbf{Y}(t) = (Y_1(t), Y_2(t), \dots, Y_K(t))^\top$  is a  $K \times 1$  vector of measurements at time  $t$  on the  $K$  individuals,  $\mathbf{X}(t, \gamma(t))$  is a  $p \times K$  matrix, each row being the values of a covariate for the  $K$  individuals,  $\mathbf{w}(t) = (w_1(t), w_2(t), \dots, w_K(t))^\top$  is a  $K \times 1$  vector comprising a temporal process for each individual, and  $\boldsymbol{\varepsilon}(t) \sim \mathcal{N}_K(0, \tau^2 \mathbf{I}_K)$ ,  $\tau^2 \in \mathbb{R}^+$ , is a white noise process for measurement error. Each element of  $\mathbf{w}(t)$  is specified as  $w_k(t) \stackrel{\text{ind}}{\sim} \mathcal{GP}(0, c_{\boldsymbol{\theta}}(\cdot, \cdot))$ , where  $c_{\boldsymbol{\theta}}(\cdot, \cdot)$  is a covariance function with parameters  $\boldsymbol{\theta} \in \Theta$ .

Let  $y_{ki}$  and  $\mathbf{x}_{ki}$  be the outcome and covariates for individual  $k$  at time point  $t_{ki}$ , respectively, so  $\{(y_{ki}, \mathbf{x}_{ki}) : k = 1, \dots, K, i = 1, \dots, T_k\}$  is the observed data. Let  $\mathbf{y}_k$  and  $\mathbf{w}_k$  be  $T_k \times 1$  vectors comprising all measurements and random effects on patient  $k$ , respectively. Forming the  $n \times 1$  vectors  $\mathbf{y} = [y_1^\top \ y_2^\top \ \dots \ y_K^\top]^\top$  and  $\mathbf{w} = [\mathbf{w}_1^\top \ \mathbf{w}_2^\top \ \dots \ \mathbf{w}_K^\top]^\top$ , and the  $n \times p$  matrix  $\mathbf{X} = [\mathbf{X}_1^\top \ \mathbf{X}_2^\top \ \dots \ \mathbf{X}_K^\top]^\top$ , where  $\mathbf{X}_k$  is the  $T_k \times p$  matrix of predictors corresponding to  $\mathbf{y}_k$ , we extend (3) to a hierarchical model with posterior distribution

$$p(\boldsymbol{\beta}, \mathbf{w}, \boldsymbol{\theta}, \tau^2 | \mathbf{y}) \propto p(\boldsymbol{\beta}, \tau^2) \times N(\boldsymbol{\beta} | \boldsymbol{\mu}_{\boldsymbol{\beta}}, \mathbf{V}_{\boldsymbol{\beta}}) \times N(\mathbf{w} | \mathbf{0}, \mathbf{C}_{\boldsymbol{\theta}}) \times N(\mathbf{y} | \mathbf{X}\boldsymbol{\beta} + \mathbf{w}, \tau^2 \mathbf{I}_n). \quad (4)$$

The covariance matrix  $\mathbf{C}_{\boldsymbol{\theta}} = \text{diag}(\mathbf{C}_{\boldsymbol{\theta}_{1,1}}, \mathbf{C}_{\boldsymbol{\theta}_{2,2}}, \dots, \mathbf{C}_{\boldsymbol{\theta}_{K,K}})$  is  $n \times n$  block-diagonal with  $\mathbf{C}_{\boldsymbol{\theta}_{k,k}} = [c_{\boldsymbol{\theta}}(t_{ki}, t_{kj})]$  as the  $T_k \times T_k$  temporal covariance matrix corresponding to individual  $k$ . Each individual is allowed its own covariance parameters,  $\boldsymbol{\theta}_k$ , and  $\boldsymbol{\theta} = \{\boldsymbol{\theta}_1, \boldsymbol{\theta}_2, \dots, \boldsymbol{\theta}_K\}$  in (4) is the collection of all the covariance kernel parameters. Applying (4) involves the determinant and inverse of  $\mathbf{C}_{\boldsymbol{\theta}}$ , which require  $\mathcal{O}(n^2)$  storage space and  $\mathcal{O}(n^3)$  floating point operations (flops). The block-diagonal structure of  $\mathbf{C}_{\boldsymbol{\theta}}$  considerably alleviates this burden since  $\det(\mathbf{C}) = \prod_{k=1}^K \det(\mathbf{C}_{\boldsymbol{\theta}_{k,k}})$  and  $\mathbf{C}^{-1} = \text{diag}(\mathbf{C}_{\boldsymbol{\theta}_{1,1}}^{-1}, \mathbf{C}_{\boldsymbol{\theta}_{2,2}}^{-1}, \dots, \mathbf{C}_{\boldsymbol{\theta}_{K,K}}^{-1})$ . This reduces the flop count from  $\mathcal{O}(n^3) = \mathcal{O}((\sum_{k=1}^K T_k)^3)$  to  $\mathcal{O}(K \sum_{k=1}^K (T_k)^3)$ , with a significant saving of calculations especially when the  $T_k$ 's are reasonably small ( $< 10^4$ ). Furthermore, each  $\mathbf{C}_{\boldsymbol{\theta}_{k,k}}$  can be computed in parallel rendering further scalability to the algorithm.

However, analyzing the Actigraph data in Section 2 will involve  $T_k > 10^5$  measurements from some individuals. Full inference will be impractical without any exploitable structure for each  $\mathbf{C}_{\boldsymbol{\theta}_{k,k}}$ . Analyzing massive spatiotemporal data has witnessed burgeoning interest and a comprehensive review is beyond the scope of this work [see, e.g., Heaton et al., 2019, and references therein]. We will pursue an approximation due to Vecchia [Vecchia, 1988] that has generated substantial recent interest [Datta et al., 2016b,a, Katzfuss et al., 2020, Katzfuss and Guinness, 2021, Peruzzi et al., 2020] in scalable Bayesian modeling.

### 3.2 Independent DAG models over individuals

We adapt Vecchia's likelihood approximation [Vecchia, 1988] to the random effects  $\mathbf{w}_k$  for each  $k = 1, 2, \dots, K$ . Beginning with the observed time points  $\{t_{k1} < t_{k2} < \dots < t_{kT_k}\}$  for individual  $k$  and the directed acyclic graphical (DAG) representation  $p(\mathbf{w}_k) = p(w_{k1}) \prod_{i=2}^{T_k} p(w_{ki} | w_{k1}, \dots, w_{k(i-1)})$ , we define

$$p(\mathbf{w}_k) \approx \tilde{p}(\mathbf{w}_k) = p(w_{k1}) \prod_{i=2}^{T_k} p(w_{ki} | \mathbf{w}_{k,N(i)}), \quad (5)$$

where  $\tilde{p}(\cdot)$  is the joint density derived from  $p(\mathbf{w}_k)$  by restricting the parents (conditional sets) of each  $w_{ki}$  in the DAG to a set  $w_{kN(i)} = \{w_{kj} : j \in N(i)\}$ , where  $N(i)$  is a set of prefixed size  $m$  comprising the  $m$  nearest neighbors of  $t_{ki}$  from the past. Thus,  $N(i) = \{t_{k(i-m)}, \dots, t_{k(i-1)}\}$  for  $i > m$  and  $N(i) = \{t_{k1}, \dots, t_{k(i-1)}\}$  for  $i \leq m$ . Such approximations yield valid probability likelihoods [Lauritzen, 1996, Stein et al., 2004, Murphy, 2012] and can be extended to stochastic processes [Datta et al., 2016b] for inference on arbitrary time points.

The connection between sparsity and conditional independence follows by writing (5) as a linear model  $\mathbf{w}_k = \mathbf{A}_k \mathbf{w}_k + \boldsymbol{\eta}_k$ , where  $\mathbf{A}_k$  is a  $T_k \times T_k$  strictly lower triangular matrix,  $\boldsymbol{\eta}_k \sim \mathcal{N}_{T_k}(\mathbf{0}, \mathbf{D}_k)$  and  $\mathbf{D}_k$  is the  $T_k \times T_k$  diagonal matrix such that  $[\mathbf{D}_k]_{ii} = d_{ii} = \text{Var}(w_{ki} | \{w_{kj}, j < i\})$  for  $i = 1, \dots, T_k$ . The DAG imposes the lower-triangular structure on  $\mathbf{A}_k$  and its  $(i, j)$ -th entry is allowed to be nonzero only for  $j \in N(i)$ . Therefore, each row of  $\mathbf{A}_k$  has at most  $m$  nonzero entries so that  $\tilde{\mathbf{C}}_k^{-1} = (\mathbf{I}_{T_k} - \mathbf{A}_k)^\top \mathbf{D}_k^{-1} (\mathbf{I}_{T_k} - \mathbf{A}_k)$  is sparse, where  $\tilde{\mathbf{C}}_k^{-1}$  is the precision matrix corresponding to  $\tilde{p}(\mathbf{w}_k)$ . Replacing  $\mathbf{C}$  with  $\tilde{\mathbf{C}}$  in (4) yields a computationally efficient hierarchical model with  $N(\prod_{k=1}^K N(\mathbf{w}_k | \mathbf{0}, \tilde{\mathbf{C}}_k))$  as the prior on  $\mathbf{w}$ .

The key observation is that the nonzero elements of the  $i$ -th row of  $\mathbf{A}_k$  is the solution  $\mathbf{a}_k$  of the  $m \times m$  linear system  $\mathbf{C}_{\theta,k}[N(i), N(i)]\mathbf{a}_k = \mathbf{C}_{\theta,k}[N(i), i]$ , where  $[\cdot, \cdot]$  indicates submatrices defined by the given row and column index sets. Obtaining the nonzero elements of  $\mathbf{A}_k$  and  $\mathbf{D}_k$  costs  $\mathcal{O}(T_k m^3)$  (scales linearly with  $T_k$ ) instead of  $\mathcal{O}(T_k^3)$  as would have been without sparsity. This cheaply delivers the quadratic form  $\mathbf{w}_k^\top \tilde{\mathbf{C}}_k^{-1} \mathbf{w}_k$  in terms of  $\mathbf{A}_k$  and  $\mathbf{D}_k$  and the determinant  $\det(\tilde{\mathbf{C}}_k) = \prod_{i=1}^{T_k} d_{ii}$  at almost no additional cost. The lower triangular matrix  $\mathbf{A}_k$  is not just sparse but also banded, with a lower bandwidth equal to  $m$ . Consequently,  $\tilde{\mathbf{C}}_k^{-1}$  is also banded with lower and upper bandwidth equal to  $m$ . This leads to further accrual of computational benefits. The overall cost is  $\mathcal{O}(\sum_{k=1}^K T_k m^3) = \mathcal{O}(nm^3)$  (linear in  $n$ ) for computing the posterior for any given values of the parameters.

### 3.3 Implementation using collapsed models

The Bayesian hierarchical model in (4), either with  $\mathbf{C}_\theta$  or with  $\tilde{\mathbf{C}}_\theta$  in the prior for  $\mathbf{w}$ , allows full posterior inference for  $\{\beta, \mathbf{w}, \theta, \tau^2\}$  using Markov chain Monte Carlo (MCMC). Gibbs sampling with random walk Metropolis steps provide full conditional distributions in closed form for  $\{\beta, \mathbf{w}\}$  and also for  $\tau^2$  with an  $\mathcal{IG}(a_\tau, b_\tau)$  prior. However, this convenience is nullified in practice by strong autocorrelation and poor mixing of the chains [Liu et al., 1994]. Samplers based on spatial DAG-based models have been devised, explored and compared in Finley et al. [2019]. Instead of (4), we sample from

$$p(\beta, \theta, \tau^2 | \mathbf{y}) \propto p(\theta, \tau^2) \times N(\beta | \mu_\beta, V_\beta) \times N(\mathbf{y} | \mathbf{X}\beta, \tilde{\mathbf{C}}_\theta + \tau^2 \mathbf{I}_n), \quad (6)$$

which is derived from (4) by integrating out  $\mathbf{w}$ , thereby “collapsing” the parameter space to a much smaller domain without  $\mathbf{w}$ . This considerably improves mixing and convergence.

We will need to compute the inverse and determinant of  $\tilde{\Lambda} = \tilde{\mathbf{C}}_\theta + \tau^2 \mathbf{I}_n$ , which is  $n \times n$ . While  $\tilde{\Lambda}^{-1}$  does not share the same convenient factorization of  $\tilde{\mathbf{C}}^{-1}$  and is also not guaranteed to be sparse, the Sherman-Woodbury-Morrison formulas reveal

$$\tilde{\Lambda}^{-1} = \tau^{-2} \mathbf{I} - \tau^{-4} \Omega^{-1}, \quad \text{with} \quad \Omega = \tilde{\mathbf{C}}^{-1} + \tau^{-2} \mathbf{I}, \quad (7)$$

where  $\Omega$  enjoys the same sparsity as  $\mathbf{C}^{-1}$ . Moreover,  $\det(\tilde{\Lambda}) = \tau^{2n} \det(\tilde{\mathbf{C}}) \det(\Omega)$ . The core of the algorithm is therefore to compute  $\tilde{\Lambda}^{-1}$  through  $\Omega$ . In our application, the random effect is assumed to be the realization of  $K$  independent temporal processes. As discussed in Section 3.2, this implies a block-diagonal structure for  $\tilde{\mathbf{C}}$  that can be shown to be shared also by  $\Omega$  (see Eq. (7)). Each block  $\Omega_k$  of  $\Omega$  can be computed independently for each individual and the same holds for its inverse and its determinant. This means that the body of the algorithm will consist of a loop over all the individuals, which allows for straightforward parallelization; see Algorithm 1. Unlike in spatial DAGs [Datta et al., 2016b, Finley et al., 2019], we do not need fill-reducing permutation methods since neighbors sets for temporal processes consist of contiguous observations and  $\{\Omega_k\}_{k=1}^K$  are banded matrices with no gaps.

We devised a Gibbs sampler with Metropolis random walk updates for (6), where  $\beta$  is updated from its full conditional distribution, while  $\{\theta, \tau^2\}$  are updated using an adaptive Metropolis step based on Haario et al. [2001]. Here, after the first few iterations, a new proposal covariance matrix is regularly computed on the run according to the empirical covariance of the current chain. Subsequently, a mixture of the original and adaptive proposal is used as the new proposal. Convergence toward the desired acceptance rate is assured for an appropriate choice of the variance terms and of the adaptation rule [Roberts and Rosenthal, 2009]. The algorithm has been coded using the R 4.0.1 statistical environment. All expensive computations are managed by the Eigen library (version 3.3.7), which provides efficient routines for numerical linear algebra with an emphasis on sparse matrices. Our implementation of (6) outperforms the algorithms that update  $\mathbf{w}$  in terms of computational speed as it is implemented in the spNNGP package [Finley et al., 2017]. We present these comparisons in the online supplement (Appendix).

### 3.4 Including spatial effects

Accounting for spatial information in our Actigraph dataset presents some new considerations. As mentioned in Section 1, spatial information is available to us in terms of the physical location along the trajectory as well as through covariates that are functions of space. Considering the discussion in Section 3, the analytical goals of this dataset suggest accounting for *spatial heterogeneity*. Here, as argued earlier, modeling  $\mathbf{w}(\cdot)$  in (3) as a spatiotemporal process, including scalable versions, has challenges given that: (i) the trajectory’s domain does not have a positive area; and (ii) associations among the measurements are more amenable to the temporal scale. Therefore, we introduce spatial effects into the mean employing a smooth function of space,  $f_S(\cdot) : \mathbb{R}^2 \rightarrow \mathbb{R}$ , approximated by a spline basis representation [see, e.g., Goodman and Hardin, 2006, Ramsay and Silverman, 2007]. For instance, if  $J_x$  and  $J_y$  are the dimensions of independently defined B-spline basis expansions on the  $x$  and  $y$  coordinates, respectively, then  $f_S((x, y)) \approx$

**Algorithm 1:** Sampling from the posterior of the collapsed temporal model

```

0: Initialization
begin
  for  $k = 1, \dots, K$  do
    a: Compute  $d_{ij}^k = |t_j - t_i|$ ,  $\forall t_j, t_i \in \mathcal{T}_k$ 
    b: Find the neighbor sets  $\{N_k(i)\}_{i=1}^{T_k}$ 
  end
begin
  1: Metropolis-Hastings update for  $\{\theta, \tau^2\}$ 
   $p(\theta, \tau^2 | \cdot) \propto p(\theta, \tau^2) \times \frac{1}{\sqrt{\det \tilde{\Lambda}}} \exp\left(-\frac{1}{2} (\mathbf{y} - \mathbf{X}\beta)^\top \tilde{\Lambda}^{-1} (\mathbf{y} - \mathbf{X}\beta)\right)$ 
  begin
    for  $k = 1, \dots, K$  do
      a: Compute  $\mathbf{L}_k = (\mathbf{I}_{T_k} - \mathbf{A}_k)^\top$ ,  $\mathbf{d}_k = \text{diag}(\mathbf{D}_k)$  and  $\mathbf{R}_k = \mathbf{D}_k^{-1} (\mathbf{I}_{T_k} - \mathbf{A}_k)$  using  $\mathbf{C}_k$  and  $\{N_k(i)\}_{i=1}^{T_k}$ 
      b: Compute  $\Omega_k = \mathbf{L}_k \cdot \mathbf{R}_k + \tau^{-2} \mathbf{I}_{T_k}$  exploiting sparsity
      c: Compute  $\mathbf{r}_k = \mathbf{y}_k - \mathbf{X}_k \beta$  and  $\delta_{\mathbf{D}_k} = \prod_{i=1}^{T_k} d_{k,i}$ 
      d: Compute  $\mathbf{v}_k = \Omega_k^{-1} \mathbf{r}_k$ ,  $\mathbf{u}_k = \Omega_k^{-1} \mathbf{X}_k$  and  $\delta_{\Omega_k} = \det(\Omega_k)$  exploiting the sparse Cholesky decomposition of  $\Omega_k$ 
      e: Collect  $\mathbf{r}_k$ ,  $\mathbf{v}_k$  and  $\mathbf{u}_k$  into  $\mathbf{r}$ ,  $\mathbf{v}$  and  $\mathbf{u}$ , respectively.
    end
    f: Compute  $q_1 = \tau^{2n} \cdot \prod_{k=1}^K \delta_{\mathbf{D}_k} \cdot \prod_{k=1}^K \delta_{\Omega_k}$  and  $q_2 = \mathbf{r}^\top \mathbf{r} / \tau^2 - \mathbf{r}^\top \mathbf{v} / \tau^4$ 
    g: Get  $p(\theta, \tau^2 | \cdot) \propto \frac{\exp(-q_2/2)}{\sqrt{q_1}} \cdot (\theta, \tau^2)$ 
  end
  2: Gibbs' sampler update for  $\beta$ 
   $\beta | \cdot \sim \mathcal{N}_p(\mathbf{B}^{-1} \mathbf{b}, \mathbf{B}^{-1})$ , where  $\mathbf{B} = \mathbf{X}^\top \tilde{\Lambda}^{-1} \mathbf{X} + \mathbf{V}_\beta^{-1}$  and  $\mathbf{b} = \mathbf{X}^\top \tilde{\Lambda}^{-1} \mathbf{y} + \mathbf{V}_\beta^{-1} \mu_\beta$ 
  begin
    a: Compute  $\mathbf{F} = \mathbf{V}_\beta^{-1}$  and  $= \mathbf{V}_\beta^{-1} \mu_\beta$ 
    b: Compute  $\mathbf{b} = \mathbf{y}^\top \mathbf{X} / \tau^2 - \mathbf{y}^\top \mathbf{v} / \tau^4 + \mathbf{F}$  and  $\mathbf{B} = \mathbf{X}^\top \mathbf{X} / \tau^2 - \mathbf{X}^\top \mathbf{v} / \tau^4 + \mathbf{F}$ 
    c: Generate  $\beta \sim \mathcal{N}_p(\mathbf{B}^{-1} \mathbf{b}, \mathbf{B}^{-1})$ 
  end
Repeat steps 1 and 2 to obtain  $M$  MCMC samples for  $\{\beta, \theta, \tau^2\}$ 

```

$\tilde{f}_S((x, y)) = \sum_{j_x=1}^{J_x} \sum_{j_y=1}^{J_y} \beta_{S,(j_x, j_y)} B_{x, j_x}(x) B_{y, j_y}(y)$ , where  $B_{x, j_x} = [\mathbf{B}_x]_{j_x}$  and  $B_{y, j_y} = [\mathbf{B}_y]_{j_y}$  are the  $j_x$ -th and  $j_y$ -th element of the B-spline basis along the two axis. For any location  $(x, y) \in \mathbb{R}^2$  the elements of the previous sum can be more compactly expressed through the tensor product basis  $\mathbf{B}_S(x, y) = (\mathbf{B}_x \otimes \mathbf{B}_y)(x, y)$ . The size of this basis is  $J_S = J_x \cdot J_y$  and depends on the size of the two original spline basis, which in turn depends on the chosen number of knots  $\text{knots}_x, \text{knots}_y$  and degree  $\text{deg}_x, \text{deg}_y$  (namely  $J_c = \text{knots}_c + \text{deg}_c$  for  $c = x, y$ ). We now modify (3) to include the spline,

$$\mathbf{Y}(t) = \mathbf{X}(t)\beta + \mathbf{B}_S(\gamma(t))\beta_S + \mathbf{w}(t) + \varepsilon(t), \quad t \in \mathbb{R}^+, \quad (8)$$

where  $\gamma(t) = \{\gamma_1(t), \gamma_2(t), \dots, \gamma_K(t)\}$ ,  $\gamma_k(\cdot) = (\gamma_{k,x}(t), \gamma_{k,y}(t)) : \mathbb{R}^+ \rightarrow \mathbb{R}^2$  is the trajectory function mapping time  $t$  for individual  $k$  to its position and  $\mathbf{B}_S(\gamma(t))$  is the  $K \times J_S$  matrix with row  $k$  corresponding to the  $J_S$  basis elements for the coordinates at time point  $t$  for individual  $k$ . A proper choice of  $J_S$  (i.e. knots and degree) is required to fit a spline surface flexible enough to describe the spatial variations at the scale of interest without incurring over-fitting. Let us denote with  $\mathbf{B} = \mathbf{B}_S(\gamma(\mathcal{T}))$  the  $n \times J_S$  matrix containing the B-spline basis elements evaluated at the observed location of each individual  $\gamma(\mathcal{T}) = \{\gamma_1(t_{11}), \gamma_1(t_{12}), \dots, \gamma_K(t_{KT_k})\}$ . Following Equation (6), we sample from the posterior,

$$p(\beta, \beta_S, \theta, \tau^2 | \mathbf{y}) \propto p(\theta, \tau^2) \times p_S(\beta_S) \times N(\beta | \mu_\beta, \mathbf{V}_\beta) \times N(\mathbf{y} | \mathbf{X}\beta + \mathbf{B}\beta_S, \tilde{\mathbf{C}}_\theta + \tau^2 \mathbf{I}_n), \quad (9)$$

where the prior  $p_S(\cdot)$  shall be accurately chosen. We must consider that our Actigraph data includes millions of observations in a limited study area, of which some assume different values in the same location (or in its immediate vicinity) so over-fitting will not be an issue. However, some areas present sparsely observed points (trajectories are not uniformly distributed, as shown in Figure 2). This may cause coefficients corresponding to those regions to be weakly identified. To control for the balance of all these components, we may assign ad-hoc priors to the spatial spline regression coefficients [Eilers and Marx, 1996] for penalizing deviation from a certain degree of smoothness and favoring identifiability. This yields the Bayesian P-Spline [Hastie et al., 2000, Lang and Brezger, 2004]. While keeping the Gaussian priors, we effectuate shrinkage by choosing a suitable precision matrix  $\mathbf{P}$  and introducing a shrinkage parameter  $\lambda$  at a deeper level of the hierarchy. To be precise,  $\beta_S | \lambda \propto \exp\left\{-\frac{\lambda}{2} \cdot \beta_S \mathbf{P} \beta_S^\top\right\}$  and  $\lambda \sim \mathcal{G}(\alpha_\lambda, \beta_\lambda)$ . We consider two possible forms for  $\mathbf{P}$ , which imply different penalization for the coefficients:

**Algorithm 2:**  $\psi$  and  $\lambda$  Gibbs' update in the collapsed algorithm with shrinkage**1: Gibbs' sampler update for  $\psi$** 
 $\psi | \cdot \sim \mathcal{N}_J(\mathbf{G}^{-1}\mathbf{g}, \mathbf{G}^{-1})$ , where  $\mathbf{G} = \mathbf{X}^{*\top} \tilde{\boldsymbol{\Lambda}}^{-1} \mathbf{X}^* + \mathbf{V}_\psi^{-1}$  and  $\mathbf{g} = \mathbf{X}^{*\top} \tilde{\boldsymbol{\Lambda}}^{-1} \mathbf{y} + \mathbf{V}_\psi^{-1} \boldsymbol{\mu}_\psi$ 
**begin**  **a:** Compute  $\mathbf{F} = \mathbf{V}_\psi^{-1}$  and  $= \mathbf{V}_\psi^{-1} \boldsymbol{\mu}_\psi$   **b:** Compute  $\mathbf{g} = \mathbf{y}^\top \mathbf{X}^* / \tau^2 - \mathbf{y}^\top \mathbf{v} / \tau^4 +$  and  $\mathbf{G} = \mathbf{X}^{*\top} \mathbf{X}^* / \tau^2 - \mathbf{X}^{*\top} \mathbf{v} / \tau^4 + \mathbf{F}$   **c:** Generate  $\psi \sim \mathcal{N}_{p^*}(\mathbf{G}^{-1}\mathbf{g}, \mathbf{G}^{-1})$ **end****2: Gibbs' sampler update for  $\lambda$** 
 $\lambda | \cdot \sim Ga(\alpha_\lambda^*, \beta_\lambda^*)$ , where  $\alpha_\lambda^* = \alpha_\lambda + 1/2$  and  $\beta_\lambda^* = \beta_\lambda + \boldsymbol{\beta}_S^\top \mathbf{P} \boldsymbol{\beta}_S$ 
**begin**  **a:** Compute  $h = \boldsymbol{\beta}_S^\top \mathbf{P} \boldsymbol{\beta}_S$  and get:  $\alpha_\lambda^* = \alpha_\lambda + 1/2$  and  $\beta_\lambda^* = \beta_\lambda + h$   **b:** Generate  $\lambda \sim \mathcal{G}(\alpha_\lambda^*, \beta_\lambda^*)$ **end**

- **Ridge-like** prior, which is to say  $\mathbf{P} = \mathbf{P}_{RL} = \mathbf{I}_{J_S}$ ;

- **First-order random walk** prior, which is to say:

$$\mathbf{P} = \mathbf{P}_{RW} : [\mathbf{P}_{RW}]_{ij} = \begin{cases} n_i & i = j \\ -1 & i \sim j \\ 0 & \text{otherwise} \end{cases}$$

where  $n_i$  is the number of neighbors of knot  $i$  and  $i \sim j$  denotes a neighboring relationship between the knots.

Both precision matrices provide a multivariate Gaussian prior distribution on the coefficients. However, the latter is improper since  $\text{rank}(\mathbf{P}_{RW}) < J_S$ . Nevertheless, if we collect the B-Spline basis elements with the other covariates as  $\mathbf{X}^* = [\mathbf{X}, \mathbf{B}]$  and stack the corresponding coefficients into the joint vector  $\psi = [\boldsymbol{\beta}, \boldsymbol{\beta}_S]$ , then the posterior distribution of the latter is a proper multivariate Gaussian with full conditional distribution  $\psi | \cdot \propto \mathcal{N}_J(\psi | \mathbf{G}^{-1}\mathbf{g}, \mathbf{G}^{-1})$ , where  $\mathbf{G} = \mathbf{X}^{*\top} \tilde{\boldsymbol{\Lambda}}^{-1} \mathbf{X}^* + \mathbf{V}_\psi^{-1}$  and  $\mathbf{g} = \mathbf{X}^{*\top} \tilde{\boldsymbol{\Lambda}}^{-1} \mathbf{y} + \mathbf{V}_\psi^{-1} \boldsymbol{\mu}_\psi$  with  $\mathbf{V}_\psi^{-1} = \text{diag}(\mathbf{V}_\beta^{-1}, \lambda \cdot \mathbf{P})$  and  $\mathbf{g} = [\boldsymbol{\mu}_\beta, \boldsymbol{\mu}_{\beta_S}]^\top = \mathbf{0}^\top$ . Moreover, the Gamma prior on  $\lambda$  implies a Gamma full-conditional distribution  $\lambda | \cdot \propto \mathcal{G}(\lambda | \alpha_\lambda + 1/2, \beta_\lambda + \boldsymbol{\beta}_S^\top \mathbf{P} \boldsymbol{\beta}_S)$ .

Estimating the model in (8) is achieved through a straightforward extension of Algorithm 1. We jointly update  $\psi$  and  $\lambda$  from their full conditional distributions. Algorithm 2 shows how the Gibbs' sampling step of Algorithm 1 can be modified to get full inference also on the spline coefficients  $\boldsymbol{\beta}_S$  and the shrinkage parameter  $\lambda$ . In practical terms, this requires  $J_S$  additional linear coefficients to be estimated, whose size  $p^* = p + J_S$  may undermine the efficiency of the algorithm. For example, calculations in Step 1b are quadratic w.r.t.  $p^* \rightarrow \mathcal{O}(np^{*2})$ . Steps 1a and 1b (i.e. the most expensive in  $p^*$ ) are executed in the first iteration and subsequently, only in those iterations where new values of  $\theta$  are accepted. When  $\theta$  is rejected, we retain in memory the previously computed value (which would stay unchanged). Thus, if we attain an optimal acceptance rate of  $\approx 20\% - 30\%$  in the Metropolis Hastings step on  $\theta$ , the computation is avoided in the majority of cases with a sensible improvement in computation time and speed.

### 3.5 Simulations

We conducted simulation experiments to evaluate the model described in Section 3.4 and compared the performance of our algorithm in terms of fitting, prediction error and computational speed with other routines available from the spNNGP package. Additional comparative experiments are provided in the supplementary material. We executed our MCMC algorithms on a computing environment equipped with 12 modern computational nodes with 16 cores each (bringing the overall number of cores to 192), roughly equivalent to 3 TeraFlop/sec, and 64Gb of RAM. Each of the following jobs, and the ones from Section 4, have been executed on a single node exploiting all 16 cores. The results presented here and in Section 4 are based upon posterior samples that were retained after diagnosing convergence using visual tools (e.g., traceplots, autocorrelation), effective sample sizes, Monte Carlo standard errors (MCSE) and other diagnostics offered by the `coda`, `mcse` and `bayesplot` packages in the R computing environment; the online supplement (Appendix) includes specific details.

Param. (True)	S-Spline		P-Spline	
	Point	Interval	Point	Interval
$\beta_{01} (-3.76)$	-3.799	(-3.846,-3.752)	-3.797	(-3.844,-3.75)
$\beta_{02} (0.65)$	0.572	(0.523,0.62)	0.575	(0.526,0.623)
$\beta_{03} (-0.60)$	-0.649	(-0.697,-0.6)	-0.646	(-0.693,-0.598)
$\beta_{04} (2.36)$	2.326	(2.277,2.374)	2.328	(2.28,2.376)
$\beta_{05} (-0.33)$	-0.359	(-0.408,-0.31)	-0.356	(-0.404,-0.308)
$\beta_1 (2.59)$	2.599	(2.59,2.608)	2.599	(2.59,2.608)
$\beta_2 (2.70)$	2.691	(2.683,2.7)	2.691	(2.683,2.7)
$\beta_3 (-0.58)$	-0.586	(-0.595,-0.577)	-0.586	(-0.595,-0.577)
$\sigma^2 (1)$	1.001	(0.973,1.032)	0.993	(0.965,1.023)
$\phi (1)$	0.994	(0.948,1.04)	1.01	(0.964,1.063)
$\tau^2 (1)$	1.001	(0.984,1.018)	1.001	(0.984,1.018)
Metric	Out-of-sample	In-sample	Out-of-sample	In-sample
Coverage	0.95	0.99	0.95	0.99
RMSPE (r)	0.07 (1.18)	0.03 (0.84)	0.07 (1.19)	0.03 (0.84)
PIW	4.66	4.44	4.66	4.44
DIC	115'543		115'556	
Fitting time (h)	2.18		2.2	

Table 2: Parameter estimates, predictive validation and fitting times (hours) on the simulated dataset for all the considered models.

We first generated  $T_k = 2 \times 10^5$  time points for  $K = 5$  individuals, where each time point  $t_{ki}$  followed exponential waiting times between observations, i.e.  $t_{ki} = \sum_{h=1}^{i-1} \delta_h$ , and  $\delta_h \stackrel{iid}{\sim} \text{Exp}(5)$ . Given the time points, we constructed spatial trajectories  $\gamma_k(\cdot)$ ,  $k = 1, \dots, K$ , by simulating  $s_k = [\gamma_k(t_{k1}), \dots, \gamma_k(t_{kT_k})]^\top$ , where subsequent components were independent Gaussian random walks over the square  $\mathcal{S} = (1, 10) \times (1, 10)$ , with the variance of each step along the horizontal and vertical axis proportional to the elapsed time between two subsequent observations. If the trajectory left the square, it was projected onto the border and the next step would resume from there. The simulated trajectories are shown in Figure 4a.

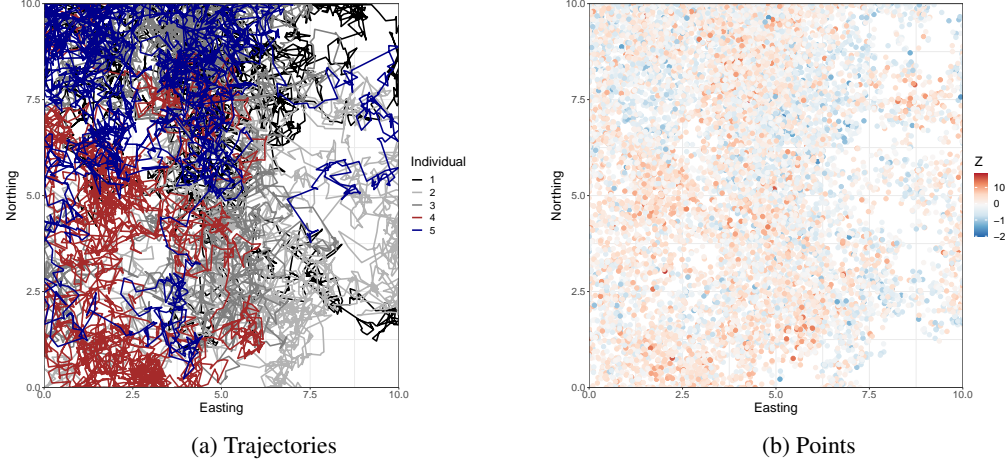


Figure 4: Observed trajectories (a) and observed points (b) for the simulated dataset.

Given the time points and positions, we generated the latent temporal Gaussian processes  $w_k(\cdot) \stackrel{iid}{\sim} \mathcal{GP}(0, c_{\theta}(\cdot, \cdot))$  with an exponential covariance  $c_{\theta}(t, t') = \sigma^2 \exp\{-\phi \cdot |t - t'|\}$ , where  $\sigma^2 > 0$  represents the variance of the process,  $\phi > 0$  is the decay in temporal correlation (range) and  $\tau^2 > 0$  the residual variance (nugget). The spatial effects are then introduced through  $f_S(\cdot) : \mathcal{S} \rightarrow \mathbb{R}$  by considering a tensor product spline basis of degree 2 and with 9 knots over the square domain (including boundary knots), where the spline coefficients  $\beta_S$  have been fixed to randomly generated values from  $\mathcal{N}_{81}(\mathbf{0}, \lambda \mathbf{I}_{81})$  with  $\lambda = 0.5$ . The model also included individual-specific intercepts  $\{\beta_{0k}\}_{k=1}^5$  and the effect of 3 covariates with random values drawn independently at each location from a  $\mathcal{N}(0, 1)$  distribution, leading to covariate vectors  $\{\mathbf{x}_{ki}\}_{i=1}^{T_k}$ ,  $k = 1, \dots, K$ . The effect of the covariates is assumed common across individuals, and set to be determined by slopes  $\beta = [\beta_1, \beta_2, \beta_3]^\top$ .

We generated values of the outcome for individual  $k$  at time  $t_{ki}$  and location  $s_{ki} = \gamma_k(t_{ki})$  according to the generative process defined by (8) with parameters fixed as above. This yielded a simulated dataset  $D_{sim} = \{(Ind_j, t_j, s_j, y_j, x_j^\top)\}_{j=1}^n$  with  $n = 10^5$  observations, where  $Ind_j$  denotes the individual corresponding to row  $j$ . Then, we fit the model in (9) on 70% of the total observations in  $D_{sim}$  using Algorithm 1 with the Gibbs' sampling modified as in Algorithm 2. The remaining 30% were held out to assess out-of-sample predictive performances in terms of *Relative and Root Mean Squared Prediction Error* (RMSPE), and *Coverage, Predictive Interval Width* (PIW). Intercept and slope regression parameters were assigned  $\mathcal{N}(0, 10^6)$  priors; the variance components,  $\sigma^2$  and  $\tau^2$ , were both assigned inverse Gamma  $\mathcal{IG}(2, 2)$  priors; and the decay parameter  $\phi$  received a Gamma prior  $\mathcal{G}(1, 1)$ . For the spline coefficients, we considered both the penalized versions in Section 3.4. The first is referred to as an S-Spline (shrinking splines), and the second as P-Spline (penalized splines).

Table 2 presents the posterior estimates. We also included the Deviance Information Criterion (DIC) for both models. Performances in the two settings are almost identical, but the DIC favors the S-Spline model. This is not surprising as the data were generated using an analogous shrinkage prior for the  $\beta_S$ 's. Further details, including the estimates of the spline coefficients are provided in the online supplement (Appendix). Figure 5 presents the posterior estimate of the spatial surface. We compare the true latent surface with the two (practically identical) estimates.

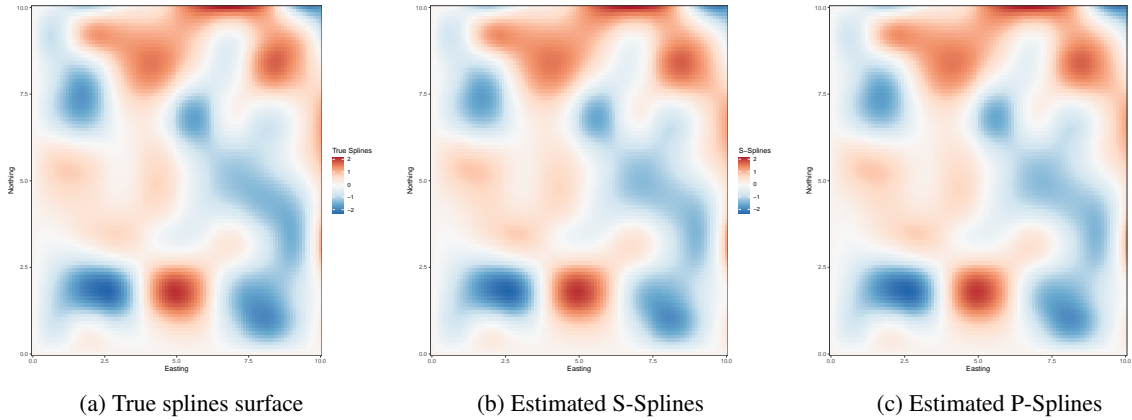


Figure 5: True (top left) and estimated spline surfaces (bottom left and right), including the point-wise difference between the true one and the S-Spline estimated (top right).

## 4 Application

We analyze activity levels throughout the “active time”—when the Actigraph device records the individual as being physically active—excluding epochs when the device was not worn or when there was no physical activity (e.g., the individual was sitting or lying down). The data processing and merging of actigraph data with GPS locations resulted in two final datasets (Section 2). These are treated separately. In both applications, 70% of the total observations were used for training the model, while the remaining were excluded to assess the out-of-sample predictive performances.

### 4.1 Temporal model

We first analyze  $D_1$ . Our predictors include a binary variable indicating if the measures refer to the period before or after a Bruin Bike Share (BBS) program was launched in Westwood, Los Angeles to account for the effect of a new specific policy which aims at improving the physical activity level of the participants. We account for the daily periodic behavior that characterizes most human activities by modeling the impact of the hour of the day on the physical activity level as a non-linear function  $f_H(\cdot) : [7, 23] \rightarrow \mathbb{R}$ , which is approximated by a linear combination of  $J_H$  spline basis functions  $\phi_j(\cdot)$  with unknown coefficients  $\beta_{H,j}$ 's,  $f_H(h) \approx \tilde{f}_H(h) = \sum_{j=1}^{J_H} \beta_{H,j} B_{H,j}(h) = \mathbf{B}_H(h)\boldsymbol{\beta}_H$ . The full process specification yields

$$\mathbf{Y}(t) = \mathbf{X}(t)\boldsymbol{\beta} + \mathbf{B}_H(h(t))\boldsymbol{\beta}_H + \mathbf{w}(t) + \boldsymbol{\varepsilon}(t), \quad t \in \mathbb{R}^+ \quad (10)$$

where  $h(\cdot) : \mathbb{R}^+ \rightarrow [7, 23]$  links each time point to the corresponding hour of the day and  $\mathbf{B}_H(\cdot) : [7, 23] \rightarrow \mathbb{R}^{J_H}$  links each hour of the day to the values of the splines at that point.

We employ a second order approximation with 4 internal knots spread uniformly over the domain. Collecting the basis elements in the design matrix and stacking the coefficients as for the spatial model in Section 3.4 introduces 6 additional columns (hence, only 6 additional slope parameters) in the design matrix (i.e. the spline basis functions evaluated at the observed time-points). The large number of observations in each epoch and the reduced number of knots subdue any concerns surrounding over-fitting and unrobust inference.

We use a logarithmic transformation,  $lMAG_k(t) = \log(MAG_k(t))$  for  $k = 1, 2, \dots, K$  and  $t = t_{k1}, \dots, t_{kT_k}$ . We denote the parameter associated with variable “varname” as  $\beta_{\text{varname}}$  and the levels of each categorical covariate as  $\text{varname}_{(j)}$  for  $j = 1, \dots, J_{\text{varname}}$ . Hence,

$$\begin{aligned} lMAG_k(t) = & \beta_0 + \beta_{\text{BMI}} \cdot \text{BMI}_k + \sum_{j=2}^{J_{\text{Sex}}} \beta_{\text{Sex},j} \cdot \mathbb{I}(\text{Sex}_k = \text{Sex}_{(j)}) \\ & + \beta_{\text{BBS}} \cdot \text{BruinBikeShare}(t) + \sum_{j=1}^{J_H} \beta_{H,j} B_{H,j}(h(t)) + w_k(t) + \epsilon_k(t), \end{aligned} \quad (11)$$

where  $\mathbb{I}(\cdot)$  denotes the indicator function,  $w_k(\cdot)$  is the DAG-based approximation (Section 3.2) for  $\mathcal{GP}(0, c_{\theta}(\cdot, \cdot))$  with  $c_{\theta}(t, t')$  the exponential function and  $\epsilon_k(t) \stackrel{\text{iid}}{\sim} \mathcal{N}(0, \tau^2)$ . For the categorical variables “Age” and “Sex”, the levels start from 2 as  $J = 1$  is taken as the baseline, which corresponds to an Asian female with age between 20 and 25 years. Other socioeconomic factors (e.g. education and income level) have been excluded from the analysis as they are strongly associated with ethnicity and age, while *Lux* (detecting light exposition) was excluded after some preliminary analysis revealed its low predictive power<sup>3</sup>. We have assigned priors such as  $\beta \sim \mathcal{N}_J(\mathbf{0}, 10^6 \cdot \mathbf{I}_J)$ ,  $\sigma^2 \sim \mathcal{IG}(2, 2)$  and  $\tau^2 \sim \mathcal{IG}(2, 2)$  with  $J$  being the total number of  $\beta$  coefficients. The presence of temporal dependence was investigated through an individual-specific exploratory analysis on the residuals from an ordinary least squares linear regression. Subsequently, it was decided that an exponential covariance function for temporal dependence (corresponding to an Ornstein-Uhlenbeck process) will be a parsimonious and effective choice to model the behavior of the underlying residual process.

We implemented Algorithm 1 for (11). Inference was based on 10,000 posterior samples retained after convergence was evinced (discarding an initial 5,000 iterations as burn-in). Point estimates from the standard linear model were used as starting values for the regression coefficients. The run time of the collapsed sampler (Section 3.3) on  $D_1$  was  $\approx 15$  hours, achieving a desirable acceptance rate of  $\approx 28\%$  at convergence.

## 4.2 Results from temporal analysis

Table 3 presents the posterior estimates. The regression coefficients were slightly different from a Bayesian linear regression model, but presented very similar inference. African Americans, Latinos and Whites revealed higher values of *lMAG* than Asian-Americans as did males over females. As expected, higher age-groups revealed lower *lMAG*. Unsurprisingly, the introduction of the temporal process effectuates slightly wider credible intervals for the regression parameters. This results in BMI being marginally less credible from the temporal process model than from linear regression. What is more surprising in both models is the slightly negative effect of BBS on physical activity. This, however, is likely a consequence of the fact that at least  $2 \cdot 10^6$  data points in  $D_1$  corresponded to individuals outside of Westwood without access to the program. The average of the *lMAG* for the reference individual is represented by the common intercept, which is estimated  $\approx 5.514$  by our model. This implies a *MAG* per minute count of 1,488, which corresponds to *hard* physical activity and an average MET of  $\approx 7$  according to the Table 1 and (2). This value, while large, is not surprising as we are modeling the epochs corresponding to active time.

The estimate of the temporal decay parameter  $\phi$ , suggests a fairly sharp decline in temporal association, which drops below 0.05 after  $\approx 1$  minute (computed, with the exponential covariance function as  $\frac{1}{3\phi}$ ). While the estimated variance of the temporal process,  $\sigma^2$ , is slightly larger than  $\tau^2$ , the latter’s estimate indicates substantial residual variation beyond the temporal process—motivating our analysis in Section 4.3. The model in (11) delivers statistical estimates (with uncertainty quantification) of personalized daily PA profiles for any individual for any day. The splines and the temporal process combine to capture subject-specific diurnal variation. Figure 6 presents the posterior estimates of daily MAGs (log) of two such individuals (number 204 (a) and 188 (b)) throughout the day to evince the inter-subject variation. This figure illustrates the need to accommodate variations among subjects when predicting their daily physical activities.

<sup>3</sup>The PASTA-LA study did not contemplate a rigorous protocol for the light exposition sensor, and hence this variable is likely to not have been recorded accurately.

Parameter	Collapsed Model		Linear regression	
	Point	Interval	Point	Interval
Intercept	5.514	(5.507, 5.520)	5.872	(5.854, 5.888)
Eth. Latin-American	0.166	(0.149, 0.183)	0.136	(0.131, 0.142)
Eth. White	0.073	(0.005, 0.095)	0.081	(0.076, 0.086)
Eth. Black or other	0.203	(0.184, 0.221)	0.164	(0.158, 0.170)
Sex Male	0.017	(0.003, 0.033)	0.023	(0.019, 0.027)
BMI	0.004	(-0.002, 0.01)	0.003	(0.002, 0.004)
Age [25-35]	-0.106	(-0.121, -0.091)	-0.124	(-0.129, -0.119)
Age [35-50]	-0.110	(-0.131, -0.09)	-0.123	(-0.129, -0.117)
Age [50-70]	-0.092	(-0.121, -0.065)	-0.144	(-0.152, -0.137)
BBS	-0.051	(-0.066, -0.037)	-0.067	(-0.071, -0.064)
$\sigma^2$	1.537	(1.528, 1.546)		
$\phi$	0.315	(0.312, 0.319)		
$\tau^2$	1.138	(1.135, 1.141)		
Metric	Out-of-sample	In-sample	Out-of-sample	In-sample
Coverage	0.94	0.97	0.94	0.94
RMSPE (r)	0.60 (1.24)	0.34 (0.93)	1 (1.59)	1 (1.59)
PIW	4.80	4.62	6.24	6.24

Table 3: Parameter credible intervals, 95%(2.5%, 97.5%) and predictive validation for  $15 \times 10^3$  MCMC iterations on  $D_1$ .

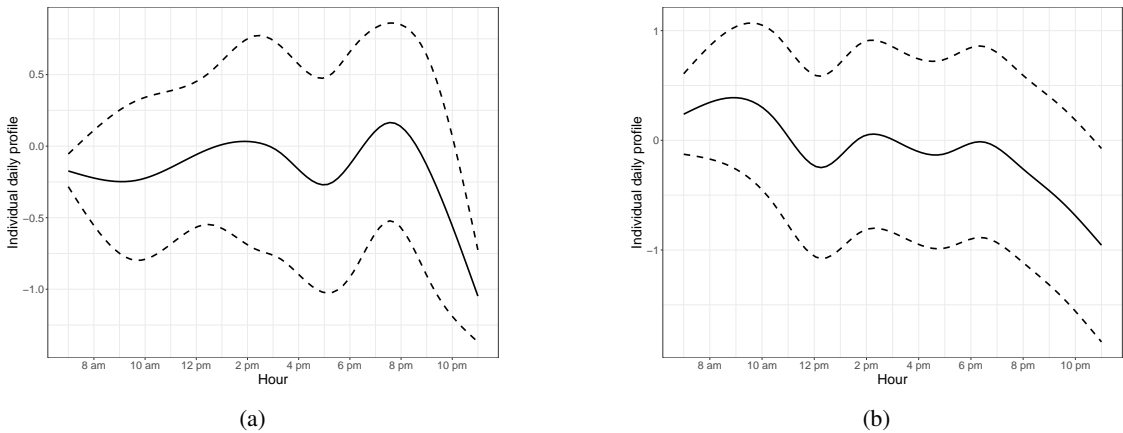


Figure 6: Personalized PA profiles for two individuals estimated with 95% credible intervals (dashed lines) using the spline daily effect and the temporal process in (11).

An example of the out-of-sample predictions of the temporal process for a set of 100 subsequent points from one specific subject (number 77) is shown in Figure 7, which demonstrates the proposed model’s ability to interpolate the IMAG values at unobserved time-points or intervals. The interpolated values (red dots) provide a slightly over-smoothed but accurate reconstruction of the held out IMAG (grey dots), which is always included in the corresponding 95% predictive bounds. This smoother behavior characterizes both in-sample and out-of-sample predictions when compared to the true values and is not necessarily a limitation of our model. Indeed, accelerations recorded by accelerometers are generally noisy, and the predicted values may be interpreted as a denoised version of the raw signal.

### 4.3 Spatial-temporal analysis

We consider  $D_2$  and fit the model in (11), adding a spatial term (Section 3.4) to exploit GPS information.  $D_2$  is restricted to those observations recorded in Westwood, Los Angeles. We introduce spatial splines obtained through the tensor product of two analogous univariate B-spline basis on longitude and latitude. We choose two bases of degree 2 with 9 equally spaced knots over a square encompassing Westwood. This sums up to  $J_S = (7 + 2) \times (7 + 2) = 81$  terms for our complete spline basis, including the boundary knots.

In practice, since locations are functions of time through the trajectory function  $\gamma_k(\cdot)$ ,  $k = 1, \dots, K$  of each individual, rewrite the time dependent component of the process mean as  $\mu_k(t) = \beta_{BBS} \cdot \text{BruinBikeShare}(t) + \sum_{j=1}^{J_H} \beta_{H,j} B_{H,j}(h(t)) + \sum_{j=1}^{J_S} \beta_{S,j} B_{S,j}(\gamma_k(t))$ , where  $B_S = B_X \otimes B_Y$  is the tensor product bivariate spline. Given the reduced number of knots and the high spatial density of observations in several areas of the map, over-fitting is not

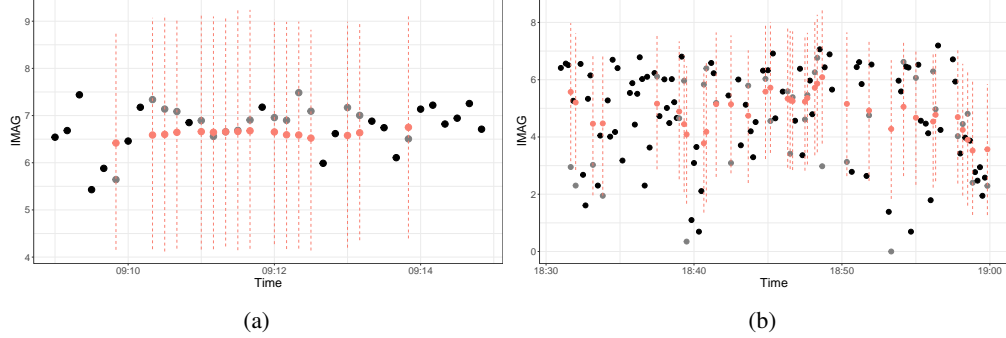


Figure 7: Out-of-sample predictions for two random individuals: black dots (observed values), grey dots (test set), pink dots (oos predictions), dashed line (95% confidence intervals)

Param.	Linear regression		S-Spline	
	Point	Interval	Point	Interval
Intercept	5.613	(5.536, 5.689)	5.31	(5.29, 5.33)
Eth. Latin-American	0.093	(0.079, 0.108)	0.114	(0.069, 0.159)
Eth. White	0.053	(0.040, 0.067)	0.053	(0.004, 0.102)
Eth. Black or other	0.066	(0.052, 0.080)	0.095	(0.054, 0.135)
Sex Male	0.019	(0.008, 0.029)	0.021	(-0.014, 0.055)
BMI	0.005	(0.003, 0.006)	0.006	(-0.007, 0.02)
Age [25-35]	-0.170	(-0.183, -0.156)	-0.191	(-0.227, -0.155)
Age [35-50]	-0.217	(-0.233, -0.201)	-0.249	(-0.298, -0.199)
Age [50-70]	-0.381	(-0.404, -0.359)	-0.456	(-0.528, -0.384)
BBS	-0.008	(-0.091, -0.071)	-0.107	(-0.140, -0.073)
$\sigma^2$			1.489	(1.461, 1.517)
$\phi$			0.364	(0.351, 0.376)
$\tau^2$			0.777	(0.768, 0.786)
Metric	Out-of-sample	In-sample	Out-of-sample	In-sample
Coverage	0.94	0.94	0.95	0.99
RMSPE (r)	0.95 (1.43)	0.95 (1.43)	0.53 (1.07)	0.26 (0.74)
PIW	5.62	5.62	4.78	4.74

Table 4: Parameter estimates and predictive validation on  $D_2$ .

a concern. However, there are also areas in Westwood that present sparsely observed data-points and the model can struggle to identify the spline coefficients referred to those areas, jeopardizing convergence of the MCMC algorithm. Therefore, we consider the S-Spline (Ridge-like prior) for this application, where the shrinkage parameter  $\lambda$  has been assigned a  $\mathcal{G}(1, 1)$  prior. Other parameters have been assigned the same priors of the temporal application in Section 4.1. Our posterior inference was based on 5,000 samples retained after convergence out of 10,000 MCMC iterations. Fitting the model to  $D_2$  required  $\approx 30$  hours. The acceptance rate obtained is  $\approx 28\%$ , supporting the consistency of our adaptive strategy.

#### 4.4 Results from spatial-temporal analysis

Table 4 presents parameter estimates and predictive performances of the model and compares with a standard linear regression model which includes the spatial spline terms, but neglects the temporal dependence structure. Conclusions on the regression coefficients are very similar to those from Section 4.1. However, accounting for the spatial effects allow for easier interpretation of the age-group regression coefficients: the older the person, the lower is the expected physical activity level. Also, both models estimate the effect of BBS as trending slightly negative. This somewhat surprising finding can be attributed to a few factors. First, the observations after the BBS launch are mostly from the winter season (February to April, the coldest months in L.A. together with December), while the others include summer and autumn (June to November, the warmest months). Given that physical activity levels tend to be lower in the colder months, there is indication of some possible confounding between the BBS effect and seasonality. Second, not all subjects were exposed to the BBS after its launch and, hence, could not take advantage of it.

In this application, the intercept is estimated to be  $\approx 5.31$  by our model and, hence, a *MAG* per minute count of 1214 (slightly lower than in the temporal application). This would again correspond to *vigorous* physical activity and a *MET* of  $\approx 6.5$ . The estimate of  $\phi$  implies that the dependence drops to 0 in less than a minute. Unsurprisingly, including the

spatial effect and the temporal process improves predictive performances (RMSPE or PIW in Table 4) over a model including only spatial effects (using linear regression with splines). The spatial-temporal model delivers satisfactory coverage and outperforms its competitor in all of the other indices for the training and testing dataset.

Figure 8a shows the estimated spatial surface, while Figure 8b presents the width of the posterior predictive intervals. The map clearly evinces zones (darker shades of red highlighted with white contours) that tend to depict high levels of physical activity. For example, the largest dark red blob in the north center-left almost perfectly tracks the UCLA campus boundary reflecting a campus environment with active mobility (walking, running, biking). Other zones of high activity identify with locations where more participants in the study live, including those residing in student dorms (northwest corner) and residential areas immediately around and in the predefined Westwood/UCLA study area (such as the south central zone) or Century City shopping center (to the east). Lighter shades (orange) correspond to areas that are less developed (open space), such as the areas in the north east; or they are areas with a high degree of transportation infrastructure and traffic (e.g., toward the western boundary). These correspond to highways (such as the Interstate-405 highway or other vehicular transportation corridors) that often have lower levels of activity because they inhibit outdoor physical activities due to noise, pollution, safety, etc. Our analysis reveals three additional high activity areas that are not gleaned from non-spatial models: the *Los Angeles National Veteran Park*; the *Century City shopping center* and the *Stone Canyon Park*. The color gradient closely follows the spatial characteristics of the Westwood neighborhood and reveal how spatial patterns can impact physical activity behavior after accounting for variation attributable to known explanatory variables.

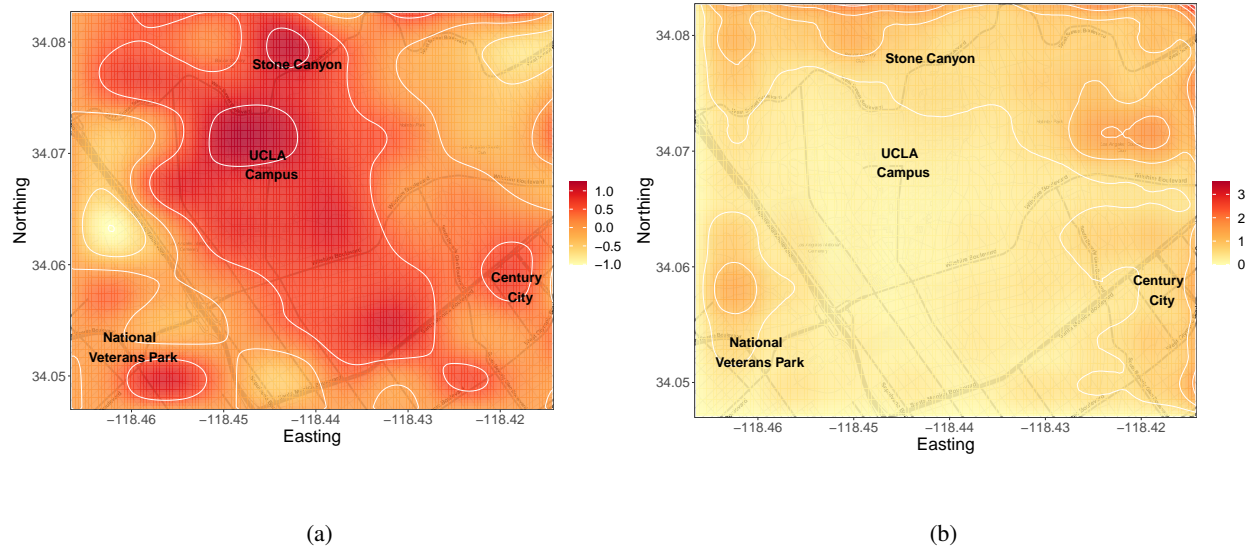


Figure 8: (a) Spatially smoothed estimates from a shrinkage spline over Westwood, Los Angeles; (b) width of 95% posterior predictive intervals for the shrinkage spline.

Figure 9 shows two examples of observed (left) and reconstructed (right) MAGs along trajectories carved out by two subjects. We find a good degree of agreement between the two plots, and the ability of our model to recover the *lMAG* in locations where it has not been observed. The reliability of the predictions can be proved through different metrics and, unsurprisingly, including the spatial effect and the temporal process improves predictive performances either in terms of MSPE or PIW. We deliver these personalized trajectory plots for every subject in the study and also predict personalized MAGs for each subject along any new trajectory. This enables personalized recommendations based upon an individual's health attributes including suggestions for more effective paths to follow for optimal physical activities, while also informing community level interventions in the built environment.

## 5 Discussion

We have devised a Bayesian modeling framework to conduct fully model-based inference for high-resolution accelerometer data over trajectories compiled from the PASTA-LA study. Our key data analytic developments included (i) modeling dependence over trajectories; (ii) accounting for subject-specific spatial-temporal variation for daily mobility;

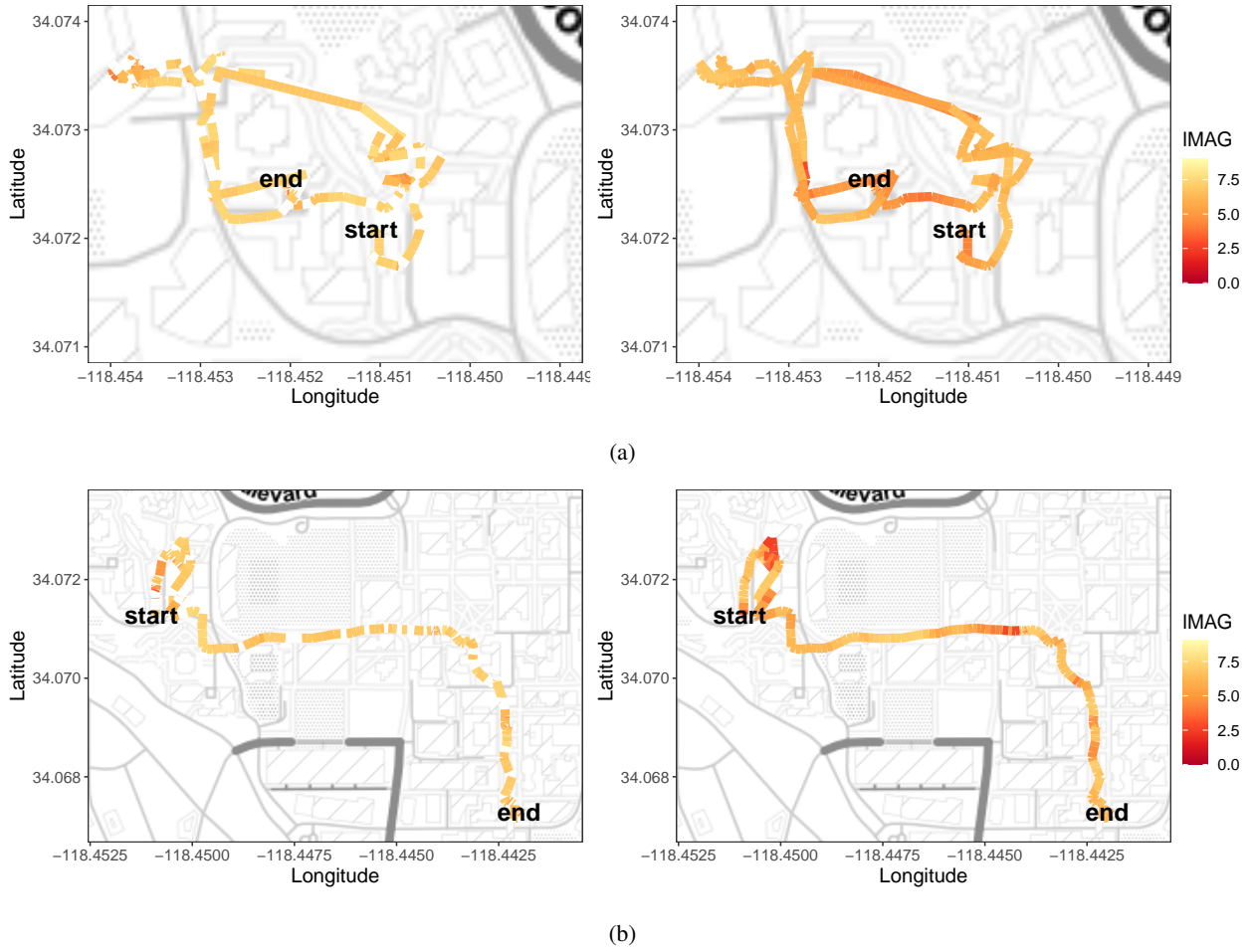


Figure 9: Two randomly chosen *lMAG* trajectories over Westwood from individual 204 (a) and individual 566 (b). Observed trajectories with gaps are seen on the left panels; spatially reconstructed (predicted) trajectories are seen on the right panels.

and (iii) predicting or interpolating PA levels across trajectories; and (iv) identify zones of high physical activity in Westwood, Los Angeles. Our spatiotemporal analysis offers richer inference and evinces relationships between physical activity levels and a variety of factors, both at the subject level (e.g., personal attributes) and as a function of space and time. The temporal process was able to effectively glean the features of the data at finer resolutions, while the spatial splines accounted for residual spatial heterogeneity. Accommodating both temporal dependence and spatial heterogeneity demonstrably improved predictive ability and enabled us to effectively delineate zones of high physical activity. Furthermore, the ability of the model to pool information across individuals at all time points allows us to infer about those who present sparsely observed space-time points (due to technical issues or protocol violation). In particular, given our improved predictive power, we can fill gaps and infer about PA levels with good accuracy and ensure the desired coverage by our prediction intervals.

Our analysis also resolves practical difficulties in using actigraph data. It is not cost-effective to deploy research-grade GlobalSat GPS and Actigraph units as they are very expensive and continued usage requires heavy staff involvement. Our methods can be applied to analogous, but less complete, data derived from smart phones and smart watches, then such devices could be deployed in much larger studies with much larger sample sizes at a fraction of the cost. Given the spatiotemporal nature of outdoor PA research, our ability to predict in areas of data missingness drastically improve inference related to the impacts of the built and natural environments on physical activity and active mobility.

While our approach offers trajectory-based inference for actigraph data, we recognize that there are several avenues for further research. Our DAG-based approach for scalable temporal processes can be further enriched with recent developments [Katzfuss and Guinness, 2021, Peruzzi et al., 2020], although any of the methods reviewed and evaluated

by Heaton et al. [2019] can be incorporated into our framework. Finally, there is possible merit in modeling the activity counts in each axis jointly and relaxing the assumptions of Gaussianity using recent developments in multivariate spatiotemporal count models and for non-Gaussian outcomes [see, e.g. Bradley et al., 2018, 2020].

Recent public health reviews call for interdisciplinary technological advances to more effectively measure spatiotemporal energetics of activity spaces in obesity and chronic disease research [James et al., 2016, Kestens et al., 2017, Drewnowski et al., 2020]. Individual-level data, at aggregate, can be used to identify anchor points for physical activity and reveal causal pathways between built environment exposures and health. Our work is a novel contribution demonstrating methodologies for how these pressing research questions may be answered.

## Supplementary Materials

The online supplement (Appendix) provides additional simulation experiments expanding upon the analysis presented here and further details on MCMC specifications. Computer programs executing the models and reproducing the analysis are also provided.

## Funding

The work of the authors have been supported in part by National Science Foundation (NSF) under grants NSF/DMS 1916349 and NSF/IIS 1562303, and by the National Institute of Environmental Health Sciences (NIEHS) under grants R01ES030210 and 5R01ES027027.

## References

Accelerometer data collection and processing criteria to assess physical activity and other outcomes: A systematic review and practical considerations. *Sports medicine*, 47(9):1821–1845, 2017. 4

Nicolas Aguilar-Farias, GMEE Peeters, Robert J Brychta, Kong Y Chen, and Wendy J Brown. Comparing actigraph equations for estimating energy expenditure in older adults. *Journal of sports sciences*, 37(2):188–195, 2019. 4

Jonathan R. Bradley, Scott H. Holan, and Christopher K. Wikle. Computationally efficient multivariate spatio-temporal models for high-dimensional count-valued data (with discussion). *Bayesian Analysis*, 13(1):253–310, 2018. 17

Jonathan R. Bradley, Scott H. Holan, and Christopher K. Wikle. Bayesian hierarchical models with conjugate full-conditional distributions for dependent data from the natural exponential family. *Journal of the American Statistical Association*, 115(532):2037–2052, 2020. doi:[10.1080/01621459.2019.1677471](https://doi.org/10.1080/01621459.2019.1677471). URL <https://doi.org/10.1080/01621459.2019.1677471>. 17

Fiona C Bull, Salih S Al-Ansari, Stuart Biddle, Katja Borodulin, Matthew P Buman, Greet Cardon, Catherine Carty, Jean-Philippe Chaput, Sebastien Chastin, Roger Chou, et al. World health organization 2020 guidelines on physical activity and sedentary behaviour. *British journal of sports medicine*, 54(24):1451–1462, 2020. 1

Noel Cressie and Christopher K Wikle. *Statistics For Spatio-Temporal Data*. John Wiley & Sons, 2011. 2

Noel Cressie and Christopher K Wikle. *Statistics For Spatio-Temporal Data*. John Wiley & Sons, 2015. 21

Scott E Crouter, Kurt G Clowers, and David R Bassett Jr. A novel method for using accelerometer data to predict energy expenditure. *Journal of applied physiology*, 100(4):1324–1331, 2006. 4

A. Datta, S. Banerjee, A. O. Finley, N. A. S. Hamm, and M. Schap. Non-separable dynamic nearest-neighbor gaussian process models for large spatio-temporal data with an application to particulate matter analysis. *Annals of Applied Statistics*, 10:1286–1316, 2016a. URL <http://dx.doi.org/10.1214/16-AOAS931>. 6

Abhirup Datta, Sudipto Banerjee, Andrew O Finley, and Alan E Gelfand. Hierarchical nearest-neighbor gaussian process models for large geostatistical datasets. *Journal of the American Statistical Association*, 111(514):800–812, 2016b. 6, 7, 21

Adam Drewnowski, James Buszkiewicz, Anju Aggarwal, Chelsea Rose, Shilpi Gupta, and Annie Bradshaw. Obesity and the built environment: A reappraisal. *Obesity*, 28(1):22–30, 2020. doi:<https://doi.org/10.1002/oby.22672>. URL <https://onlinelibrary.wiley.com/doi/abs/10.1002/oby.22672>. 2, 17

Paul HC Eilers and Brian D Marx. Flexible smoothing with b-splines and penalties. *Statistical science*, pages 89–102, 1996. 8

A Finley, A Datta, and S Banerjee. Spnngp: Spatial regression models for large datasets using nearest neighbor gaussian processes. *R package version 0.1*, 1, 2017. 7, 19

Andrew O Finley, Sudipto Banerjee, and Alan E Gelfand. spbayes for large univariate and multivariate point-referenced spatio-temporal data models. *arXiv preprint arXiv:1310.8192*, 2013. 21

Andrew O Finley, Abhirup Datta, Bruce D Cook, Douglas C Morton, Hans E Andersen, and Sudipto Banerjee. Efficient algorithms for bayesian nearest neighbor gaussian processes. *Journal of Computational and Graphical Statistics*, pages 1–14, 2019. 7, 21

Patty Freedson, Heather R Bowles, Richard Troiano, and William Haskell. Assessment of physical activity using wearable monitors: Recommendations for monitor calibration and use in the field. *Medicine and science in sports and exercise*, 44(1 Suppl 1):S1, 2012. 4, 5

Alan E Gelfand, Peter Diggle, Peter Guttorp, and Montserrat Fuentes. *Handbook of Spatial Statistics*. CRC press, 2010. 2

Tim Goodman and Doug Hardin. Refinable multivariate spline functions. In *Studies in Computational Mathematics*, volume 12, pages 55–83. Elsevier, 2006. 7

Heikki Haario, Eero Saksman, Johanna Tamminen, et al. An adaptive metropolis algorithm. *Bernoulli*, 7(2):223–242, 2001. 7

Katherine S Hall, Cheryl A Howe, Sharon R Rana, Clara L Martin, and Miriam C Morey. Mets and accelerometry of walking in older adults: Standard versus measured energy cost. *Medicine and science in sports and exercise*, 45(3):574, 2013. 4

Trevor Hastie, Robert Tibshirani, et al. Bayesian backfitting (with comments and a rejoinder by the authors. *Statistical Science*, 15(3):196–223, 2000. 8

Matthew J Heaton, Abhirup Datta, Andrew O Finley, Reinhard Furrer, Joseph Guinness, Rajarshi Guhaniyogi, Florian Gerber, Robert B Gramacy, Dorit Hammerling, Matthias Katzfuss, et al. A case study competition among methods for analyzing large spatial data. *Journal of Agricultural, Biological and Environmental Statistics*, 24(3):398–425, 2019. 6, 17

Peter James, Marta Jankowska, Christine Marx, Jaime E. Hart, David Berrigan, Jacqueline Kerr, Philip M. Hurvitz, J. Aaron Hipp, and Francine Laden. “spatial energetics”: Integrating data from gps, accelerometry, and gis to address obesity and inactivity. *American Journal of Preventive Medicine*, 51(5):792–800, 2016. ISSN 0749-3797. doi:<https://doi.org/10.1016/j.amepre.2016.06.006>. URL <https://www.sciencedirect.com/science/article/pii/S0749379716302276>. 2, 17

Masamitsu Kamada, Eric J Shiroma, Tamara B Harris, and I-Min Lee. Comparison of physical activity assessed using hip-and wrist-worn accelerometers. *Gait & posture*, 44:23–28, 2016. 4

Matthias Katzfuss and Joseph Guinness. A general framework for vecchia approximations of gaussian processes. *Statist. Sci.*, 36(1):124–141, 02 2021. doi:[10.1214/19-STS755](https://doi.org/10.1214/19-STS755). URL <https://doi.org/10.1214/19-STS755>. 6, 16

Matthias Katzfuss, Joseph Guinness, Wenlong Gong, and Daniel Zilber. Vecchia approximations of gaussian-process predictions. *Journal of Agricultural, Biological and Environmental Statistics*, 25:383–414, 2020. 6

Yan Kestens, Rania Wasfi, Alexandre Naud, and Basile Chaix. “contextualizing context”: Reconciling environmental exposures, social networks, and location preferences in health research. *Current Environmental Health Reports*, 4: 51–60, 2017. doi:<https://doi.org/10.1007/s40572-017-0121-8>. 2, 17

Stefan Lang and Andreas Brezger. Bayesian p-splines. *Journal of computational and graphical statistics*, 13(1): 183–212, 2004. 8

Steffen L Lauritzen. *Graphical Models*, volume 17. Clarendon Press, 1996. 6

Jun S Liu, Wing Hung Wong, and Augustine Kong. Covariance structure of the gibbs sampler with applications to the comparisons of estimators and augmentation schemes. *Biometrika*, 81(1):27–40, 1994. 7

Kate Lyden, Sarah L Kozey, John W Staudenmeyer, and Patty S Freedson. A comprehensive evaluation of commonly used accelerometer energy expenditure and met prediction equations. *European journal of applied physiology*, 111 (2):187–201, 2011. 5

Kate Lyden, Sarah Kozey Kadle, John Staudenmayer, and Patty S Freedson. A method to estimate free-living active and sedentary behavior from an accelerometer. *Medicine and science in sports and exercise*, 46(2):386, 2014. 4

Alexander HK Montoye, Rebecca W Moore, Heather R Bowles, Robert Korycinski, and Karin A Pfeiffer. Reporting accelerometer methods in physical activity intervention studies: A systematic review and recommendations for authors. *British journal of sports medicine*, 52(23):1507–1516, 2018. 5

Kevin P Murphy. *Machine Learning: A Probabilistic Perspective*. MIT press, 2012. 6

Alise E Ott, Russell R Pate, Stewart G Trost, Dianne S Ward, and Ruth Saunders. The use of uniaxial and triaxial accelerometers to measure children’s “free-play” physical activity. *Pediatric Exercise Science*, 12(4):360–370, 2000. [4](#)

Michele Peruzzi, Sudipto Banerjee, and Andrew O. Finley. Highly scalable bayesian geostatistical modeling via meshed gaussian processes on partitioned domains. *Journal of the American Statistical Association*, 0(0):1–14, 2020. doi:[10.1080/01621459.2020.1833889](https://doi.org/10.1080/01621459.2020.1833889). URL <https://doi.org/10.1080/01621459.2020.1833889>. [6](#) [16](#)

Neil E Peterson, John R Sirard, Pamela A Kulpok, Mark D DeBoer, and Jeanne M Erickson. Inclinometer validation and sedentary threshold evaluation in university students. *Research in nursing & health*, 38(6):492, 2015. [3](#)

Katrina L Piercy, Richard P Troiano, Rachel M Ballard, Susan A Carlson, Janet E Fulton, Deborah A Galuska, Stephanie M George, and Richard D Olson. The physical activity guidelines for americans. *Jama*, 320(19):2020–2028, 2018. [1](#)

Guy Plasqui and Klaas R Westerterp. Physical activity assessment with accelerometers: An evaluation against doubly labeled water. *Obesity*, 15(10):2371–2379, 2007. [2](#)

James O Ramsay and Bernard W Silverman. *Applied Functional Data Analysis: Methods and Case Studies*. Springer, 2007. [7](#)

Miriam Reiner, Christina Niermann, Darko Jekauc, and Alexander Woll. Long-term health benefits of physical activity—a systematic review of longitudinal studies. *BMC public health*, 13(1):1–9, 2013. [1](#)

Gareth O Roberts and Jeffrey S Rosenthal. Examples of adaptive mcmc. *Journal of Computational and Graphical Statistics*, 18(2):349–367, 2009. [7](#)

Alejandro Santos-Lozano, F Santin-Medeiros, Greet Cardon, Gema Torres-Luque, R Bailon, C Bergmeir, Jonatan R Ruiz, Alejandro Lucía Mulas, Nuria Garatachea, et al. Actigraph gt3x: validation and determination of physical activity intensity cut points. 2013. [4](#)

Jeffer E Sasaki, Dinesh John, and Patty S Freedson. Validation and comparison of actigraph activity monitors. *Journal of science and medicine in sport*, 14(5):411–416, 2011. [4](#)

Robby S Sikka, Michael Baer, Avais Raja, Michael Stuart, and Marc Tompkins. Analytics in sports medicine: Implications and responsibilities that accompany the era of big data. *JBJS*, 101(3):276–283, 2019. [2](#)

Michael L Stein, Zhiyi Chi, and Leah J Welty. Approximating likelihoods for large spatial data sets. *Journal of the Royal Statistical Society: Series B (Statistical Methodology)*, 66(2):275–296, 2004. [6](#)

Kristin Taraldsen, Sebastien FM Chastin, Ingrid I Riphagen, Beatrix Vereijken, and Jorunn L Helbostad. Physical activity monitoring by use of accelerometer-based body-worn sensors in older adults: A systematic literature review of current knowledge and applications. *Maturitas*, 71(1):13–19, 2012. [4](#)

Aldo V Vecchia. Estimation and model identification for continuous spatial processes. *Journal of the Royal Statistical Society: Series B (Methodological)*, 50(2):297–312, 1988. [6](#)

## Appendix

### 6 Additional simulation experiments

We carried out two additional experiments to test the reliability of our algorithm and verify comparative performances with the Sequential NNGP as it is implemented in the *spNNGP* package [Finley et al., 2017]. We did not consider the Response NNGP because it does not recover the latent component. The first one is described in Section 6.1 and includes simulated observations for one single individual; the second one includes simulated observations for multiple individuals and is described in Section 6.2.

#### 6.1 Experiment 1

We generated observations  $\{y(t_j)\}_{j=1}^T$  for  $K = 1$  individual, using  $T = 10^5$  time-points, where each  $t_i = \sum_{h=1}^{i-1} \delta_h$ , and  $\delta_h \sim \text{Exp}(5)$ ,  $\forall h$ . The model included an intercept  $\beta_0$  and 3 covariates,  $x_1$ ,  $x_2$  and  $x_3$  all drawn from  $\mathcal{N}(0, 1)$ , with associated slopes  $\beta_1$ ,  $\beta_2$  and  $\beta_3$ . We modeled the covariance structure between any two simulations at time-points  $t$  and  $t'$  using the exponential covariance function:

$$\text{Cov}_{\theta} [Y(t), Y(t')] = c_{\theta}(t, t') = \sigma^2 e^{(\phi|t-t'|)}, \quad \sigma^2, \phi \in \mathbb{R}^+, \quad (12)$$

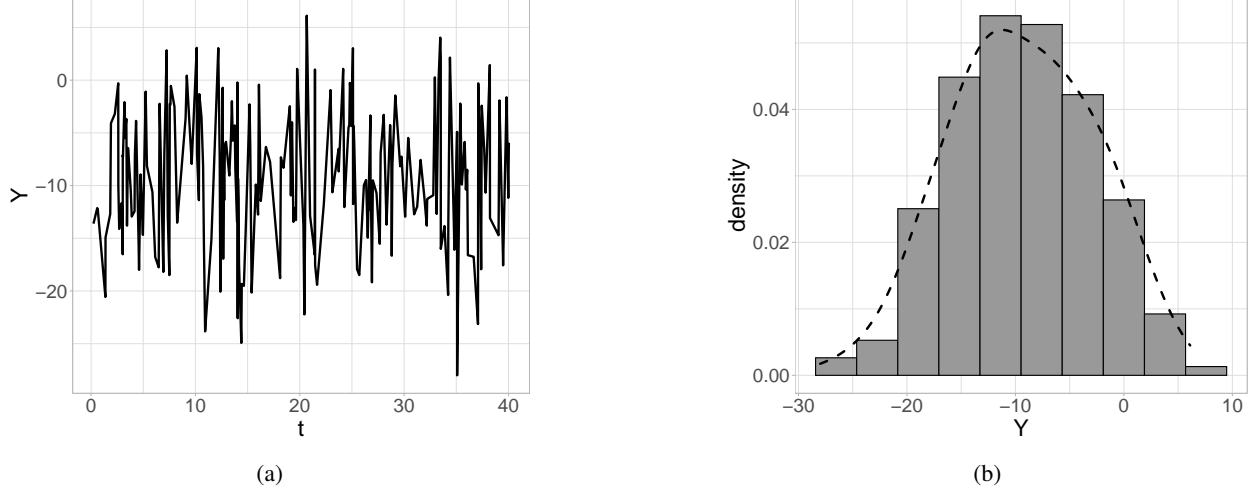


Figure 10: Simulated uni-dimensional Gaussian process (a) and its density (b).

Param. (True)	Collapsed NNGP			Sequential NNGP		
	Point	Interval	ESS	Point	Interval	ESS
$\beta_0$ (-1.88)	-1.87	(-1.89, -1.85)	4999	-1.87	(-1.89, -1.85)	57
$\beta_1$ (0.33)	0.33	(0.32, 0.34)	4999	0.33	(0.32, 0.34)	1285
$\beta_2$ (-0.30)	-0.30	(-0.31, -0.29)	4999	-0.30	(-0.31, -0.3)	1365
$\beta_3$ (1.18)	1.18	(1.17, 1.19)	4999	1.18	(1.17, 1.19)	1342
$\sigma^2$ (1)	1.00	(0.97, 1.03)	472	1.00	(0.97, 1.03)	294
$\phi$ (1)	0.99	(0.95, 1.04)	496	0.99	(0.95, 1.04)	65
$\tau^2$ (1)	1.01	(0.99, 1.03)	457	1.01	(0.99, 1.03)	165
Metric	Out-of-sample	In-sample		Out-of-sample	In-sample	
Coverage	0.95	0.99		0.96	0.99	
RMSPE (r)	0.39 (1.19)	0.20 (0.85)		0.39 (1.19)	0.20 (0.85)	
PIW	4.68	4.46		4.78	4.47	
Run time (h)	1.77			1.86		

Table 5: Parameter estimates, predictive validation and fitting times (hours) on the simulated dataset for all the considered models.

where  $\sigma^2$  represents the variance of the process (sill),  $\phi$  is the decay in temporal correlation (range) and  $\tau^2$  the residual variance (nugget). In this data generation step the parameters have been set to the following values:  $\beta_0 = -1.878$ ,  $\beta_1 = 0.326$ ,  $\beta_2 = -0.302$ ,  $\beta_3 = 1.182$ ,  $\sigma^2 = \phi = \tau^2 = 1$ . A chunk of the simulated trajectory and its density can be observed as an example in Figures 10a and 10b, respectively.

We fitted the model on the simulated data using our *Collapsed NNGP* implementation, specifically optimized for the temporal setting, while fitting the *Sequential NNGP* using the *spNNGP* package. The latter, while generally used for fitting spatial (i.e. two-dimensional) models, can be adapted to the temporal (uni-dimensional) case by providing a set of locations where  $t$  is one of the coordinates and the other is fixed to a constant value (e.g.  $\{\tilde{s}_j\}_{j=1}^n = \{(t_j, 0)\}_{j=1}^n$ ). In our implementation, the intercept and slope regression parameters were given a vague normal prior distribution  $\mathcal{N}(0, 10^6)$ . The variance components,  $\sigma^2$  and  $\tau^2$ , were both assigned an inverse Gamma prior  $\text{IG}(2, 2)$ , and the decay parameter  $\phi$  was ascribed a  $\mathcal{G}(1, 1)$ . On the other hand, the *spNNGP* assumes a flat prior on the intercept and slope coefficients and a uniforma  $\mathcal{U}(a, b)$  prior on the decay parameter  $\phi$ . In this experiment we fixed  $a = 0.5$  and  $b = 30$ . All the models were trained on the same random sample composed of the 70% of the total observations, while the remaining 30% have been excluded to assess the out-of-sample predictive performances in terms *Relative Mean Squared Prediction Error* (RMSPE), *Root Mean Squared Prediction Error* (rMSPE), *Coverage*, *Predictive Interval Width* (PIW).

We ran the 10000 MCMC iterations, fixing the number of neighbours  $m = 10$ . The first 5000 simulations have been dropped as burn-in, while the last 5000 have been retained for estimation and prediction purposes. No thinning has

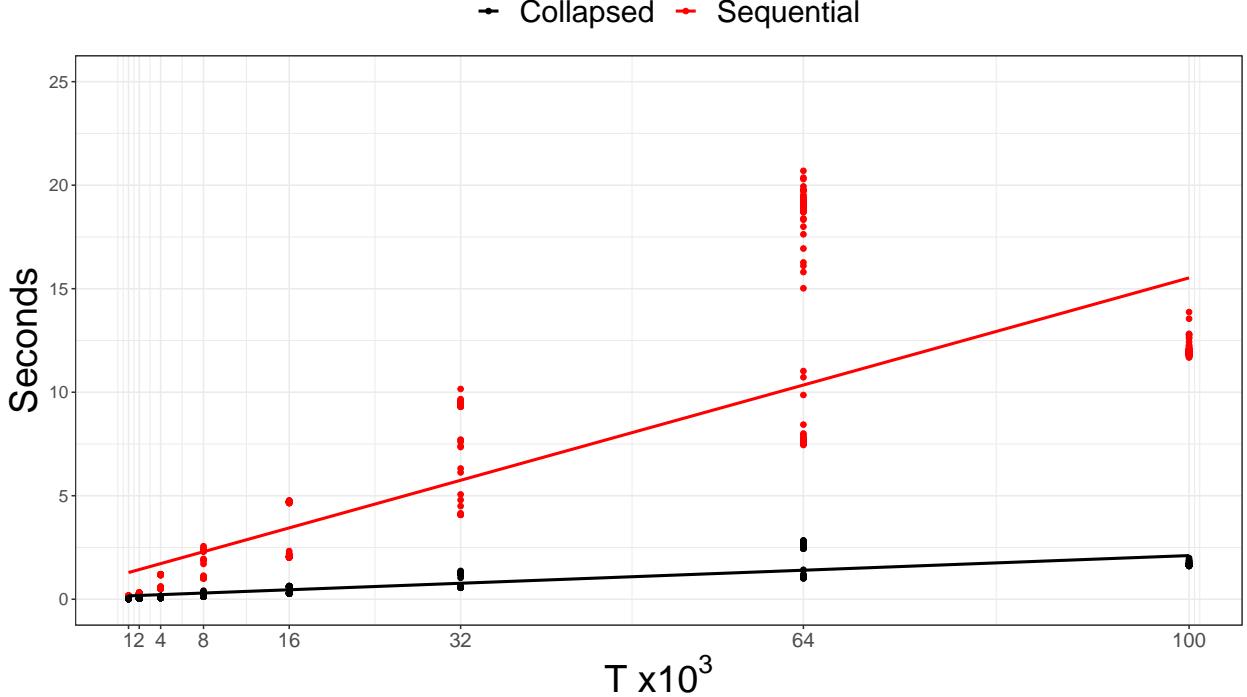


Figure 11: Time elapsed (in seconds) for 1 MCMC iteration for the two considered algorithms with increasing sample size  $T$  and fixed  $m = 30$ .

been considered. Results are summarized in Table 5. The two approaches provide identical outputs, both in terms of estimation and prediction. However, our implementation is faster than its competitor (at least in the context of the temporal setting) and provides way better performances in terms of Effective Sample Size (ESS).

### 6.1.1 Computation time evaluation

In order to delve more into the computational aspect, we *quantified* the *linearity* of all the algorithms: by construction, the fitting time should increase linearly with the sample size. We split observations in  $l = 1, \dots, 5$  different fitting windows  $\{t_1, \dots, t_{T_l}\}$  with increasing sizes  $T_l = \{\{2^l\}_{l=0}^6 \cup \{100\}\} \times 10^3$  and the computation time of one sampler iteration, fixing  $m = 30$  for all the considered algorithms has been recorded for  $\tilde{M} = 100$  times. Figure 11 shows that all algorithms scale linearly with the sample size. However, our implementation of the collapsed NNGP, whilst pointed out as generally less efficient than its competitors in [Finley et al. \[2019\]](#), scales with a rate of  $\approx 0.376 \cdot 10^{-4}$  per data-point, while the Sequential NNGP scale with a rate equal to  $\approx 4.5736 \cdot 10^{-4}$ , which is sensibly higher. For an exact numerical analysis, results are reported in Table 6.

Additionally, we wanted to quantify the computational advantage of the proposed NNGP-based collapsed algorithm over the standard MCMC update of the full GP model [[Cressie and Wikle, 2015](#)], where the latter is already implemented in R through `spLM()` function of the `spBayes` package [[Finley et al., 2013](#)]. Since [Datta et al. \[2016b\]](#) proved that the NNGP approximation with 30 neighbours provides almost exactly the same inference of the full GP, we fixed  $m = 30$  and built again different sets of data with increasing number of data-points, but this times with  $T_l = 100, 1000, 5000, 10000$  (sizes have been reduced to comply with the slow update of the Full GP). Results, which are summarized in Figure 12, showed that for  $T_l = 100$  the computational time difference between the full GP and the collapsed NNGP is negligible. However, as the size increases, the saving of time increases exponentially: 15 seconds (per iteration) when  $n = 5000$ , 122 seconds per iteration when  $n = 10000$ . For the last scenario, which is the more realistic in a MCMC inference context, this means that the collapsed NNGP will provide us with the same results 14 days in advance with respect to the Full GP model.

$T \times 10^3$	Algorithm	Min	$q_{025}$	Median	Mean	$q_{975}$	Max
1	Collapsed	0.01	0.01	0.02	0.02	0.03	0.03
	Sequential	0.12	0.12	0.13	0.14	0.18	0.18
2	Collapsed	0.03	0.03	0.03	0.04	0.06	0.07
	Sequential	0.25	0.25	0.26	0.27	0.31	0.34
4	Collapsed	0.06	0.06	0.07	0.09	0.16	0.16
	Sequential	0.50	0.50	0.52	0.64	1.21	1.21
8	Collapsed	0.13	0.14	0.30	0.26	0.32	0.41
	Sequential	1.01	1.01	2.34	1.99	2.41	2.56
16	Collapsed	0.27	0.28	0.60	0.46	0.63	0.64
	Sequential	2.02	2.02	4.65	3.46	4.75	4.77
32	Collapsed	0.55	0.56	1.23	1.17	1.28	1.37
	Sequential	4.08	4.09	9.40	8.87	9.59	10.16
64	Collapsed	1.01	1.03	2.46	1.90	2.79	2.85
	Sequential	2.51	7.49	18.71	14.43	20.13	20.69
100	Collapsed	1.60	1.61	1.67	1.68	1.87	1.99
	Sequential	11.68	11.74	11.93	12.01	12.80	13.87

Table 6: Time (in seconds) of one MCMC iteration for the two considered algorithms with increasing sample size ( $T$ ) and fixed  $m = 30$ .

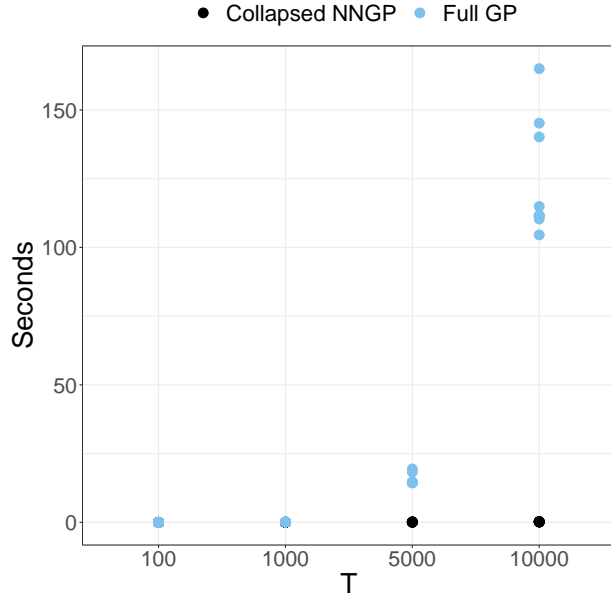


Figure 12: Time elapsed (in seconds) for 1 MCMC iteration for the Collapsed NNGP and the Full GP with increasing sample size  $T$ .

## 6.2 Experiment 2

The aim of this experiment is to verify the ability of our algorithm in recovering the true parameters and to determine if pooling information from multiple individuals can help in improving the accuracy of the estimates. Comparison with the *Sequential NNGP* is not feasible, since it does not allow the contemporary fitting of multiple Gaussian processes with common parameters. Thus, we compare performances of the Pooled NNGP (that's how we will refer to the proposed collapsed in what follows) with the single models estimated separately for each individual.

We generated  $2 \cdot 10^4$  observations for  $K = 5$  individuals, using the same scheme of Experiment 1 (total of  $10^5$  data-points). Results are presented in Table 7. The model also included 3 covariates and an intercept for each individual

drawn from independent  $N(0, 1)$ . Observations were then generated as described in Section 6.1. The simulated data was split into two sets: 70% composed the train set for estimation purposes, while the remaining 30% was used to assess model predictive performances. RMSPE, coverage of the predictive 95% credible intervals and their mean width were used as measures of the goodness of fit. For all the models, the intercept and slope regression parameters were given a flat normal prior distribution  $\mathcal{N}(0, 10^6)$ . The variance components,  $\sigma^2$  and  $\tau^2$ , were both assigned an inverse Gamma  $\mathcal{IG}(2, 2)$  priors, and the decay parameter  $\phi$  received a Gamma prior  $\mathcal{G}(1, 1)$ . The advantage of pooling information from multiple individuals for the estimation of common parameters, while the independence assumption among them still holds, is evident according to all criteria. First of all, there is a sensible gain in the estimation accuracy of the common parameters. Indeed, while the true value of the parameters are included in the intervals also considering one single individual at a time, the widths of 95% credible intervals are sensibly smaller when we pool information together. Furthermore, some slight advantage is also visible for prediction purposes, where the Pooled NNGP provides larger coverage and smaller RMSPE. Additionally, thanks to parallelization of the code, there is almost no loss in terms of the computational time required for the fitting:  $\approx 40$  minutes to fit one individual VS  $\approx 55$  minutes to fit the pooled model.

Param.	True	Pooled NNGP	Individuals				
			1	2	3	4	5
$\beta_{01}$	-9.39	-9.41 (-9.46, -9.37)	-9.41 (-9.46, -9.37)	1.59 (1.54, 1.64)	-1.54 (-1.58, -1.49)	5.91 (5.86, 5.96)	-0.81 (-0.86, -0.76)
$\beta_{02}$	1.63	1.59 (1.54, 1.64)					6.49(6.47,6.51)
$\beta_{03}$	-1.51	-1.53 (-1.57, 1.48)					6.76(6.74,6.78)
$\beta_{04}$	5.91	5.91 (5.86, 5.96)					
$\beta_{05}$	-0.82	-0.80 (-0.85, -0.76)					
$\beta_1$	6.48	6.48 (6.47, 6.49)	6.48(6.46,6.5)	6.48(6.46,6.50)	6.48(6.46,6.50)	6.46(6.44,6.48)	
$\beta_2$	6.76	6.75 (6.74, 6.76)	6.74(6.72,6.76)	6.75(6.74,6.77)	6.75(6.73,6.77)	6.75(6.73,6.77)	
$\beta_3$	-1.46	-1.46 (-1.47, -1.45)	-1.47(-1.49,-1.45)	-1.48(-1.50,-1.46)	-1.47(-1.48,-1.45)	-1.47(-1.47,-1.45)	-1.47(-1.49,-1.45)
$\sigma^2$	1	0.98 (0.96, 1.01)	0.94(0.88,1.00)	1.02(0.953,1.085)	0.93(0.88,0.99)	1.03(0.97,1.1)	1.01(0.94,1.08)
$\phi$	1	1.01 (0.97, 1.06)	1.00(0.91,1.11)	1.03(0.93,1.14)	1.06(0.95,1.17)	0.94(0.85,1.04)	0.99(0.9,1.11)
$\tau^2$	1	1 (0.99, 1.02)	1.04(1.00,1.08)	0.98(0.94,1.02)	1.00(0.967,1.04)	1.00(0.96,1.04)	0.99(0.95,1.03)
Coverage							
RMSPE	0.012 (0.006)	0.02 (0.01)	0.02 (0.01)	0.02 (0.01)	0.02 (0.01)	0.02 (0.01)	0.02 (0.01)
rMSPE	1.22 (0.84)	1.24 (0.83)	1.24 (0.83)	1.22 (0.85)	1.22 (0.85)	1.22 (0.85)	1.23 (0.84)
PIW	4.67 (4.44)	4.99 (4.44)	4.94 (4.43)	4.93 (4.43)	4.93 (4.43)	4.95 (4.44)	4.94 (4.44)
Fitting time	0.59	0.33	0.30	0.35	0.34	0.37	

Table 7: Parameter estimates (95% credible intervals), *out-of-sample* prediction error and fitting times (hours) on the simulated dataset for the pooled and the single models.